Hydrophysiology NMR reveals mechanisms of steady-state water exchange in neural tissue

Nathan H. Williamson[1,c *], **Rea Ravin**[1,2 *], **Teddy X. Cai**[1,3], **Julian A. Rey**[1,4], **and Peter J. Basser**[1] ✉

[1] *Eunice Kennedy Shriver* National Institute of Child Health and Human Development, National Institutes of Health, Bethesda, MD 20892, USA
[2] Celoptics, Rockville, MD 20850, USA
[3] Wellcome Centre for Integrative Neuroimaging, FMRIB, Nuffield Department of Clinical Neurosciences, University of Oxford, Oxford OX39DU, UK
[4] National Institute of General Medical Sciences, National Institutes of Health, Bethesda, MD 20892, USA
[c] Current address: Military Traumatic Brain Injury Initiative, Henry M. Jackson Foundation for the Advancement of Military Medicine, Bethesda, Maryland, USA
[*] N.H.W. and R.R. contributed equally to this work.

SUMMARY

Water molecules exchange incessantly across cell membranes and among different environments within the cell, but it is not known what the dominant transport pathways are and whether they are active or passive. We have developed realtime NMR hydrophysiology methods to study steady-state water exchange and diffusion in viable *ex vivo* neonatal mouse spinal cord samples. We find that water exchange is not active but is linked to tonicity maintained by active transport. Exchange slows following sodium–potassium pump inhibition but recovers to a normal rate after adding extracellular osmolytes. Additional information from apparent water diffusion coefficients (ADC) differentiates normal and inactive samples regardless of tonicity. Data and modeling suggest a multisite exchange mechanism in which tonicity modulates the dominant apparent exchange pathway between fast transmembrane exchange and slow intracellular exchange. The transmembrane pathway has a high activation energy but does not require ions, suggesting that in this pathway exchange likely occurs through the lipid bilayer rather than through channels or cotransporters. These methods may one day be translated to clinical MRI scanners to determine features of the cellular state *in vivo*.

steady state water exchange, homeostasis, diffusion exchange spectroscopy, DEXSY, tissue microstructure, porous media, membrane permeability, low-field single-sided NMR, apparent diffusion coefficient, ADC, gray matter

Correspondence: ***basserp@mail.nih.gov***

Introduction

Most of the brain's energy budget is devoted to homeostasis — maintaining states conducive to normal cellular, tissue and organ function.[1] The full characterization of cell volumes, pressures, membrane potentials, and water and ion concentrations which define a state, as well as the electrochemical potential through which they are coupled, is of high interest, but achieving such a characterization is extremely challenging, generally requiring invasive measurements.[2,3] However, gradients in these parameters establish the driving forces for transport of permeable molecules (e.g., water and ions) across cell membranes. Thus, it may be possible to noninvasively determine features of the cellular state by measuring the resulting transmembrane transport of endogenous molecules.

The permeability of the plasma membrane necessitates that molecules, including water, are always exchanging between inside and outside the cell, even at steady-state (i.e., when there is no net flux). This is quantified by the rate constant for apparent steady-state water exchange, hereafter called the "exchange rate", k. While the apparent value can vary depending on measurement parameters (e.g., gradient strengths and timings/durations)[4], in isolated cells, k has been shown to depend on diffusive permeability κ_d and the membrane surface-to-volume ratio SVR through the relation[5]

$$k = \kappa_d \mathrm{SVR}. \tag{1}$$

This is in the case of barrier-limited exchange, where water molecules tend to diffuse across the cell many times before exiting.[6] Research is on-going to understand the determinants of k in heterogeneous[7] and metabolically-active[8–16] tissues such as central nervous system (CNS) gray matter[17,18]. Nonetheless, from the prevalence of dendrites, unmyelinated axons, and glial cell processes with sub-micron diameter plasma membranes[19] composed of polyunsaturated lipids and cholesterol[20–22], we expect that $\mathrm{SVR} \gtrsim 1\ \mu\mathrm{m}^{-1}$ and $\kappa_d \approx 100\ \mu\mathrm{m/s}$. This leads to the prediction that k could be greater than $100\ \mathrm{s}^{-1}$ in gray matter.

Nuclear magnetic resonance (NMR) can characterize diffusion and the steady-state exchange of water noninvasively.[23] Magnetic field gradients can be used to encode for molecular displacements along the direction of the gradient and to measure the apparent diffusion coefficient (ADC).[24] Differences in diffusion properties within the intracellular and extracellular environments can be observed on timescales where water on average has felt the effect of plasma membranes but has not yet permeated them. On these timescales, water inside cells is less mobile because it is bounded and restricted by membranes, whereas water outside is more mobile because it can diffuse through a tortuous and narrow but connected extracellular space (ECS). In this way the ADC may be used as a proxy for cell volume,[25–27] but not necessarily quantitatively due to structural heterogeneity. In particular, the heterogeneity of cell size and the orientation of cellular processes can lead to water in some intracellular domains appearing more mobile than others. Exchange between environments where water mobility differs can be measured by encoding the same water at two instances separated by a mixing time during which the water can communicate between environments.[4,28–30] In this way, the exchange rate is sensitive to membrane permeability (through Eq. 1). However,

estimating κ_d from k is complicated by the heterogeneity of cell SVRs and the presence of other exchange pathways, such as between regions inside the cell.

The temperature dependence of water exchange rates have been used to measure activation energies (E_a).[31] While most studies report E_a values consistent with those expected for membrane permeability,[5,29] an additional mechanism is required to explain reports of E_a varying with cellular state.[8,16] Sensitivity of the exchange rate to pharmacological inhibitors and cellular energetics suggested a second mechanism involving active transporters,[32] in particular the Na^+/K^+–ATPase.[9–16] Researchers hypothesized a mechanism referred to as "active water cycling" involving water moving in tandem with ions through transporters.[11,12] A similar water cotransport mechanism was found to exist for the case of net water flux[33–37] but has not been demonstrated for steady-state water exchange. Elucidating the transport mechanisms that govern water exchange will advance our understanding of cellular homeostasis in the CNS and augment the potential utility of NMR-based water exchange measurements as indicators of cell status.

In this paper, we demonstrate in viable *ex vivo* CNS gray matter that active water cycling is not a major component of steady-state water exchange. Instead, the main determinant of k is the osmotic pressures exerted on the plasma membranes, established by the transporters. These pressures define the tonicity, or partitioning of water between the intra- and extracellular spaces. Data and modeling suggest that k is sensitive to at least two competing pathways for water exchange, which are modulated by tonicity. A fast pathway that dominates under isotonic and hypertonic conditions is associated with a high E_a and does not require extracellular NaCl. This rules out cotransporters (which require ions) and channels (which have lower E_a). We therefore ascribe this fast exchange pathway to transport across the lipid bilayer. A slow pathway has a lower E_a, similar to water self-diffusion, and dominates during hypotonic conditions. We interpret this pathway as exchange between environments within the cell, such as between cell bodies and processes or along branching processes. With additional information from the ADC, we find signatures of homeostatic volume regulation as cells resist tonicity changes. This allows us to differentiate normal and inactive samples regardless of the tonicity, which suggests a path forward for imaging the functional state of neural tissue. Exchange rates could offer a potential quantitative functional imaging biomarker which could have profound consequences for our understanding of cell status in health and disease.

Methods

Ethics statement for animal experimentation. All experiments were carried out in compliance with the *Eunice Kennedy Shriver* National Institute of Child Health and Human Development Animal Care and Use Committee under Animal Study Proposal (ASP) # 21-025.

Details of NMR and tissue preparation methods can be found in Refs. 30,38, and 16, and are described briefly here.

Mouse spinal cord sample preparation and experimental conditions. All experiments were performed on Swiss Webster wild type mice (Taconic Biosciences, Rensselaer, NY, USA) between postnatal day 1 and 4. The mouse spinal cords were isolated in a dissecting chamber perfused with low-calcium, high-magnesium artificial cerebrospinal fluid (aCSF), with the same composition as normal aCSF (listed below) but 0.5 mM $CaCl_2 \cdot 2H_2O$ and 6 mM $MgSO_4 \cdot 7H_2O$, bubbled with 95% O_2/5% CO_2. After dissection, the spinal cord was placed in the sample chamber in normal calcium aCSF, composed of 128.35 NaCl, 4 KCl, 1.5 $CaCl_2 \cdot 2H_2O$, 1 $MgSO_4 \cdot 7H_2O$, 0.58 $NaH_2PO_4 \cdot H_2O$, 21 $NaHCO_3$, 30 D-glucose (concentrations in mM), bubbled with 95% O_2 and 5% CO_2. aCSF flowed through the chamber at 7 mL/min. Chemical perturbations performed in this study included adding the pharmacological Na^+/K^+–ATPase inhibitor ouabain (European Pharmacopeia Reference Standard), adding osmolytes sucrose or mannitol (Sigma Aldrich), and switching between media in which the 128.35 mM NaCl was replaced with 256.7 mM sucrose or 128.35 mM sodium gluconate (Sigma Aldrich). Switching between media involved washing in an open loop with 100 mL of new media. Sample temperature was monitored by a fiber optic sensor (PicoM, Opsens Solutions Inc., Québec, Canada) and was controlled by water circulating through heat exchangers connected to a chiller. The sample temperature was maintained at $25 \pm 0.2°C$ by manually regulating the temperature of the chiller. Temperature perturbations were performed by rapidly (5 min equilibration) switching between $25 \pm 0.2°C$ and $11 \pm 0.2°C$ using three-way valves upstream and downstream of the chamber connected to two chillers set at different temperatures.

NMR hardware, experimental protocol, and analysis methods. NMR experiments were performed with a single-sided permanent magnet[39] (PM10 NMR MOUSE, Magritek, Aachen Germany) at magnetic field strength $B_0 = 0.3239$ T and gradient strength $g = 15.3$ T/m. A test chamber and radiofrequency (RF) probe with a solenoid coil were specially built to maintain live sample viability and maximize filling factor and SNR.[16,30]

NMR experimental protocols involved looping through sets of diffusion experiments, rapid diffusion exchange experiments, and T_1 saturation recovery experiments. Each set took 11 minutes to acquire. Diffusion experiments were performed using a standard spin echo sequence[40] and 4-step phase cycle[41]. The diffusion encoding time, τ of the spin echo was varied linearly from 0.05 to 3.3 ms over 22 steps with 4 scans per τ. This corresponds to b-values ranging from 0.001 to 400 $\mathrm{ms}/\mu\mathrm{m}^2$ where $b = 2/3\gamma^2 g^2 \tau^3$ and γ is the gyromagnetic ratio.[42] Points two through four ($\tau = 0.2048$ to 0.5143 ms, $b = 0.096$ to $1.5\ \mathrm{ms}/\mu\mathrm{m}^2$) of diffusion data were fit with $I(b) = I_0 \exp(-b\,\mathrm{ADC})$ to estimate the ADC and I_0, the MR signal in the absence of diffusion weighting. For measurements on spinal cords, the term ADC_y is used, acknowledging that diffusion may be anisotropic but was measured only along the y direction, perpendicular to the cord.

Rapid diffusion exchange experiments were performed fol-

lowing the Diffusion Exchange Ratio (DEXR) method[6] using a diffusion exchange spectroscopy (DEXSY) sequence involving two spin echoes separated by a mixing time t_m in the presence of a static magnetic field gradient[30] and a 4-step phase cycle[43]. Experiments were performed with (τ_1, τ_2) combinations (0.200, 0.735) ms and (0.593, 0.580) ms, and 8 scans per combination. The t_m values were [0.2, 1, 2, 4, 7, 10, 20, 40, 80, 160, 300] ms. The signal from $(\tau_1, \tau_2) =$ (0.200, 0.735) was fit with $I(t_m) = I_0(w_1 \exp(-t_m R_1^1) + (1 - w_1)\exp(-t_m R_1^2)$. The resulting model was divided out of the signal from the (τ_1, τ_2) =(0.593, 0.580) experiment and the remaining signal was fit with $I(t_m) = I_0 \exp(-t_m k) + B$ to estimate the exchange rate, k (similar to Method 3 in Ref. 38).

Experimental design and statistical analysis . Hypothesis tests of whether MR metrics were affected by perturbations were performed using paired-sample t-tests, with $p < 0.05$ deemed as significant.

Simulation methods. The pump–leak model (PLM) of cell volume maintenance provided by Kay (2017) was used to predict how perturbations affect cell volume and transmembrane potential.[44] The PLM approximates intracellular ion concentration and volume changes over time from the active flux of Na^+ and K^+ by the Na^+/K^+–ATPase pump and passive fluxes of Na^+, K^+, and Cl^-. The model assumes electroneutrality and zero transmembrane osmolarity gradient. The simulated cell contains a set amount of negatively-charged intracellular impermeant species to model the average osmotic effect of metabolites, proteins, nucleic acids, and other molecules trapped inside the cell. The cell is isolated in a bathing media. The normal media condition was defined as $Na_o = 128$ mM, $K_o = 4$ mM, and $Cl_o = Na_o + K_o = 132$ mM based on the aCSF composition but neglecting divalent cations and glucose. Values of volume and transmembrane voltage were taken once the system reached steady-state (if applicable). The Na^+/K^+–ATPase pump rate for the "PUMP ON" condition was defined as the value which maintained a transmembrane voltage $V = -48$ mV under normal conditions. This voltage was previously measured by intracellular recording from motoneurons in the *ex vivo* neonatal mouse spinal cord.[45] In normal media and with the PUMP OFF condition, the PLM predicts cell volume to increase towards infinity and voltage to decrease towards zero without reaching steady-state due to the imbalanced osmotic pressure from intracellular impermeants.

A three-site exchange model was developed to predict how perturbations affect the extracellular space (ECS) fraction (f_o), ADC, and k. This model improves on the PLM by including an osmotic pressure from trapped ECS impermeants and a fixed total volume equal to the sum of extracellular space and intracellular space volumes (ECS + ICS = w_{tot}). The fixed volume imposes a rigid boundary condition which limits the maximum extent of cell swelling ($f_o = 0$). The osmotic pressure of ECS impermeants is equal to the hydrostatic pressure exerted onto the rigid boundary. This effectively accounts for the dura surrounding the spinal cord which holds the tissue together. These improvements lead to a stable cell volume with the PUMP OFF due to the ECS osmotic pressure increasing as the cells swell and ECS shrinks. However, it is a steady-state model and assumes the voltage to be a fixed input value. We used -48 mV for PUMP ON conditions (based on intracellular recordings discussed above) and -10 mV for the PUMP OFF conditions (Based on recordings under hypoxic or terminal depolarization in various CNS tissue models[46]). The model involves first setting an initial f_o for the normal cell condition. Here, $f_o = 0.3$ was chosen based on tetramethylammonium real-time iontophoresis measurements of 0.27 in the P8–10 mouse spinal cord slice model and the trend towards larger ECS fraction in younger animals.[19,47] Then, an analytical equation based on an osmolarity balance was used to predict f_o for the media and PUMP ON/OFF conditions (Eq. S1).

The three sites or compartments in the exchange model were a less mobile ICS compartment (**a**), a more mobile ICS compartment (**b**), and an ECS compartment (**c**). ADC was modeled as the sum of the ADCs of each compartment multiplied by their relative volume fractions[27]. k was modeled by simulating DEXR data using an operator formalism[48–51] and then fitting the exchange model discussed above. The operator formalism involved an exchange matrix (Eq. 1) with a transmembrane exchange rate between ECS and both ICS compartments (k_t) and geometric exchange rate between ICS compartments (k_g). Transmembrane and geometric exchange rates were determined by the Arrhenius model (Eq. 3) using $E_a = 52$ kJ/mol for transmembrane and $E_a = 22$ kJ/mol for geometric, based roughly on the extremes of the experimental data, and A values defined by the EEC function (Eq. 4) with $\ln(A') = 2.18 \ln(s^{-1})$ and $T_c = -17.1°C$ found experimentally (presented in Fig. 7). See the supplement for additional PLM and three-site exchange model details.

Results

Sodium–potassium pump inhibition with ouabain has a large effect on exchange rate and simultaneously a smaller effect on apparent diffusion coefficient. First, we demonstrate results of simultaneous realtime NMR hydrophysiology measurements of k and ADC_y during perturbations with ouabain. Here, the subscript "y" refers to the gradient (and hence diffusion encoding) direction, which is perpendicular to the orientation of the spinal cord.

Ouabain is a specific inhibitor of the Na^+/K^+–ATPase. Previous studies have used the strong effect of ouabain on exchange rate as evidence for active water cycling.[11,12] We reproduced and built on those studies by examining the effects of varying ouabain dosage. We investigated the effects of 100 μM ouabain, which is expected to maximally inhibit the Na^+/K^+–ATPase, as well as the effects of 2 and 10 μM ouabain, which are expected to result in partial inhibition.[52] Ouabain simultaneously decreased ADC_y and k (Fig. 1 A, B, D, E and Fig. S1). ADC_y and k were affected within 11 minutes after the addition of 100 μM ouabain (Fig. 1 A, D, G, and H) and did not recover when the drug was washed

out (Fig. 1 A and D). The effect on k was precipitous, dropping over a duration of 11 minutes or less, limited by the temporal resolution of realtime recording (Fig. 1 D, G and H). At 10 μM ouabain, the effect was delayed but still precipitous (Fig. 1 G and H). At 2 μM ouabain, the effect was delayed further but always occurred within 200 min of addition (Fig. 1 B, E, G and H). The effect of 2 μM was precipitous in some cases (Fig. 1 B and E) but less so overall (Fig. 1 G). Subsequent exposure to higher ouabain concentrations did not produce any further effect (Fig. 1 B and E). Nevertheless, the impact of the initial dose of ouabain on ADC_y was influenced by the concentration (Fig. 1 C). 2, 10 and 100 μM ouabain decreased ADC_y by $5.6 \pm 3.1\%$, $8.6 \pm 1.8\%$, and $10.5 \pm 2.2\%$, respectively (significantly different between groups, $p < 0.001$, see Fig. 1 C). In comparison, k was much more affected by ouabain, but it depended less on the dosage. k is $131 \pm 19\ \mathrm{s}^{-1}$ under normal conditions. Ouabain reduced k by $72 \pm 7\%$ (averaged across the three concentration groups, Fig. 1 F). 2 μM ouabain reduced k to $43.8 \pm 6.8\ \mathrm{s}^{-1}$ (significantly different from the other concentration groups, $p < 0.001$). 10 and 100 μM ouabain reduced k to 35.2 ± 6.0 and $35.6 \pm 8.2\ \mathrm{s}^{-1}$ respectively (not significantly different, $p = 0.857$). The similar precipitous but delayed effect across dosages (with only a small difference at the lowest 2 μM concentration) is reminiscent of an "all-or-none" effect. The coincident effect on ADC_y suggests that cells were swelling when the drop in k occurred. Simulations also predict that deactivating the $\mathrm{Na}^+/\mathrm{K}^+$ pump causes cell swelling and membrane depolarization due to the redistribution of ions (Fig. S2).

We tested whether there was a correlation between k and ADC_y. First, the relative change from baseline of $\Delta\mathrm{ADC}_y$ and Δk are plotted for all measurements in the ouabain treated groups (Fig. 1 F inset). The correlation is significant but weak (correlation coefficient $cc = 0.45$, $p < 0.001$) and is insignificant when the 2 μM data is omitted ($p = 0.7$). A linear fit of the data yields $\Delta k = 1.05 \times \Delta\mathrm{ADC}_y - 63.0\ \%$. The correlation suggests that perhaps some of the k variation may be described by factors also affecting ADC_y. However, the y-intercept is shifted well below 0, indicating that these factors alone cannot account for the effect of ouabain on k. Second, the data is grouped based on whether ouabain was administered and correlations between the absolute values of ADC_y and k are presented. The two groups do not share the same correlation (Fig. 1 I). ADC_y and k showed a weak positive correlation before the effect of ouabain ($cc = 0.32$, $p < 0.001$) and a weak negative correlation after ouabain took effect ($cc = -0.21$, $p = 0.03$). Note that the correlation seen when plotting ADC_y percent changes from baseline appears much different than when plotting the absolute values (compare Fig. 1 F inset to Fig. 1 I). Weak and different correlations between the groups (i.e., with or without ouabain) suggest that underlying tissue properties affect k and ADC_y differently. Previous studies used similar results as evidence of active water cycling.[11,12] However, it is difficult to completely rule out the possibility that these results could be explained by more complicated microstructural effects since activity and microstructure are interlinked normally and are both affected by $\mathrm{Na}^+/\mathrm{K}^+$–ATPase inhibition.

Exchange rate is not directly linked to ion transport, voltage, or active water cycling. Certain cotransporters have been shown to cotransport water with ions.[33–37] A similar mechanism involving water actively cycling along with ions through cotransporters downstream of the $\mathrm{Na}^+/\mathrm{K}^+$–ATPase was proposed to explain the effect of ouabain on k.[11,12] Here we further test this hypothesis by studying the effects of pump inhibition independent from microstructure. Since cells pump ions to control tonicity and cell volumes under normal conditions,[44] we used an osmolyte to compensate for tonicity changes induced by pump inhibition. Specifically, we used an aCSF media in which the major ionic component, 128.35 mM NaCl, was replaced with 256.7 mM sucrose (Fig. 2 A and B). This media recipe was inspired by electrophysiology studies which use 0 NaCl, high sucrose media to maintain viability of adult animal brain slices.[53] Compared to normal aCSF, the 0 NaCl, 256.7 mM sucrose media has an equal osmolarity but a higher tonicity because sucrose remains extracellular, while Na^+ and Cl^- are not exclusively extracellular (Fig. S2).

The 0 NaCl, 257 mM sucrose media caused $\Delta\mathrm{ADC}_y$ to increase by $2.1 \pm 1.3\%$ because its higher tonicity shrunk cells slightly (Fig. 2 A and E). If water actively cycles along with ions, then k would decrease when washing to 0 NaCl, 257 mM sucrose media because $\mathrm{Na}^+/\mathrm{K}^+$ pump activity is effectively extinguished. Instead, k increased by $27 \pm 24\%$ and 10 μM ouabain had no additional effect (Fig. 2 A and F). When ouabain was added first, the 0 NaCl, 257 mM sucrose media added subsequently returned k to levels observed prior to ouabain administration (Fig. 2 B and F). Therefore, k is not linked to ion transport or $\mathrm{Na}^+/\mathrm{K}^+$ pump activity *per se*, but rather to the tonicity which is established by its activity.

In a related experiment, normal aCSF media was washed to media in which the 128.35 mM NaCl was replaced with 128.35 mM sodium gluconate. Gluconate is a monovalent anion and does not pass through the plasma membrane.[54] Due to electroneutrality, for every anion of gluconate in the ECS there will also be a cation (ignoring divalent cations). Therefore, 128.35 mM sodium gluconate adds 256.7 mOsm of osmotic pressure. The resulting pressure is the same as replacing 128.35 mM NaCl with 256.7 mM sucrose. Simulations predict that cells can maintain voltage polarization with this media, but unlike in normal media, they depolarize *without* a change in volume when the $\mathrm{Na}^+/\mathrm{K}^+$ pump is inactivated (Fig. S2). This is because gluconate does not flow into the cell following the loss of membrane potential as chloride would. In this way, the use of sodium gluconate media can help distinguish effects related to voltage from effects related to cell volume.[54]

We found that washing to sodium gluconate media had no significant effect on $\mathrm{ADC_y}$ or k (Fig. 2 C, E, and F). Adding 10 μM ouabain on top of sodium gluconate media caused $\mathrm{ADC_y}$ to increase, indicating cellular shrinkage. It also caused k to increase to values similar to those obtained under 0 NaCl, 257 mM sucrose media conditions. This is expected

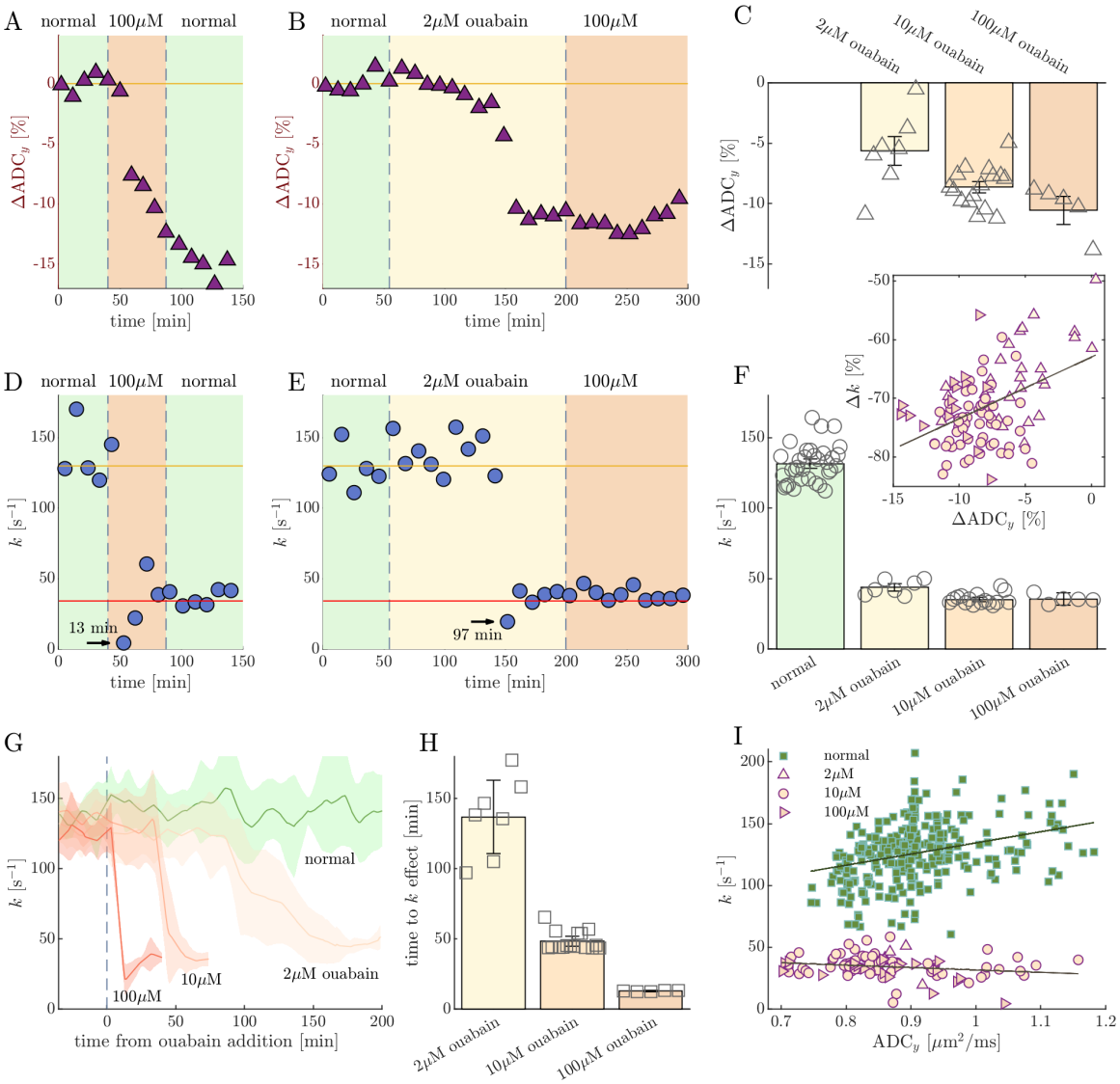

Fig. 1. Sodium–potassium pump inhibition with ouabain has a large effect on exchange rate and simultaneously a smaller effect on ADC. A,B,D,E) Representative real-time recordings on individual samples show how ouabain in (A,D) high (100 μM) and (B,E) low (2 μM) concentrations affects (A,B) ADC in the y-direction (presented as % change from baseline, $\Delta\mathrm{ADC}_y$) and (D,E) exchange rate (k). In (D) and (E), arrows and text show when k decreased below 60 s^{-1} and the time from ouabain addition to the effect. C,F) Bar graphs of (C) $\Delta\mathrm{ADC}_y$ and (F) k, showing the mean across all measurements (bar height), 95% CI of the mean (whiskers), and mean values from each sample (open symbols) for the normal condition, 2, 10, and 100 μM ouabain (n =33, 7, 16, and 5 respectively). For ouabain conditions, data was compiled from the first 3 to 5 measurements after an effect was observed and did not incorporate data from additional treatments or doses. F-inset) The correlation between $\Delta\mathrm{ADC}_y$ and Δk for all measurements in the 2, 10, and 100 μM ouabain-treated groups (right-pointing triangles, circles, and up-pointing triangles, respectively). G) Mean (solid lines) and standard deviation (shaded regions) of realtime exchange rate measurements from a control group under normal conditions (green) and groups treated with 2, 10, and 100 μM ouabain (lightest to darkest colors) plotted against the time after addition of ouabain. H) Bar chart of the time from ouabain addition to the time at which k dropped below 60 s^{-1}. I) Correlation plot of ADC_y vs. k. Data was grouped based on whether measurements occurred before (normal) or after 2, 10, and 100 μM ouabain affected k (see legend).

based on the similar osmolarities of these medias, but it further implies that cells were regulating their volume[55] while the $\mathrm{Na}^+/\mathrm{K}^+$–ATPase was still active during the sodium gluconate media condition. There was also some increase in the data variability which could be due to slow changes occurring during the measurement and the system not being at a true steady-state. Similar results were obtained when ouabain was added before washing to sodium gluconate media (Fig. 2 D, E, and F). Overall, these results indicate that k is related to volumetric conditions or tonicity but is not directly linked to ion transport, voltage, or active water cycling.

Exchange rate depends on tonicity. Next, we study the effects of osmolytes (sucrose and mannitol) on ADC_y and k under normal conditions as well as after ouabain administration. The Van't Hoff equation predicts a linear relationship

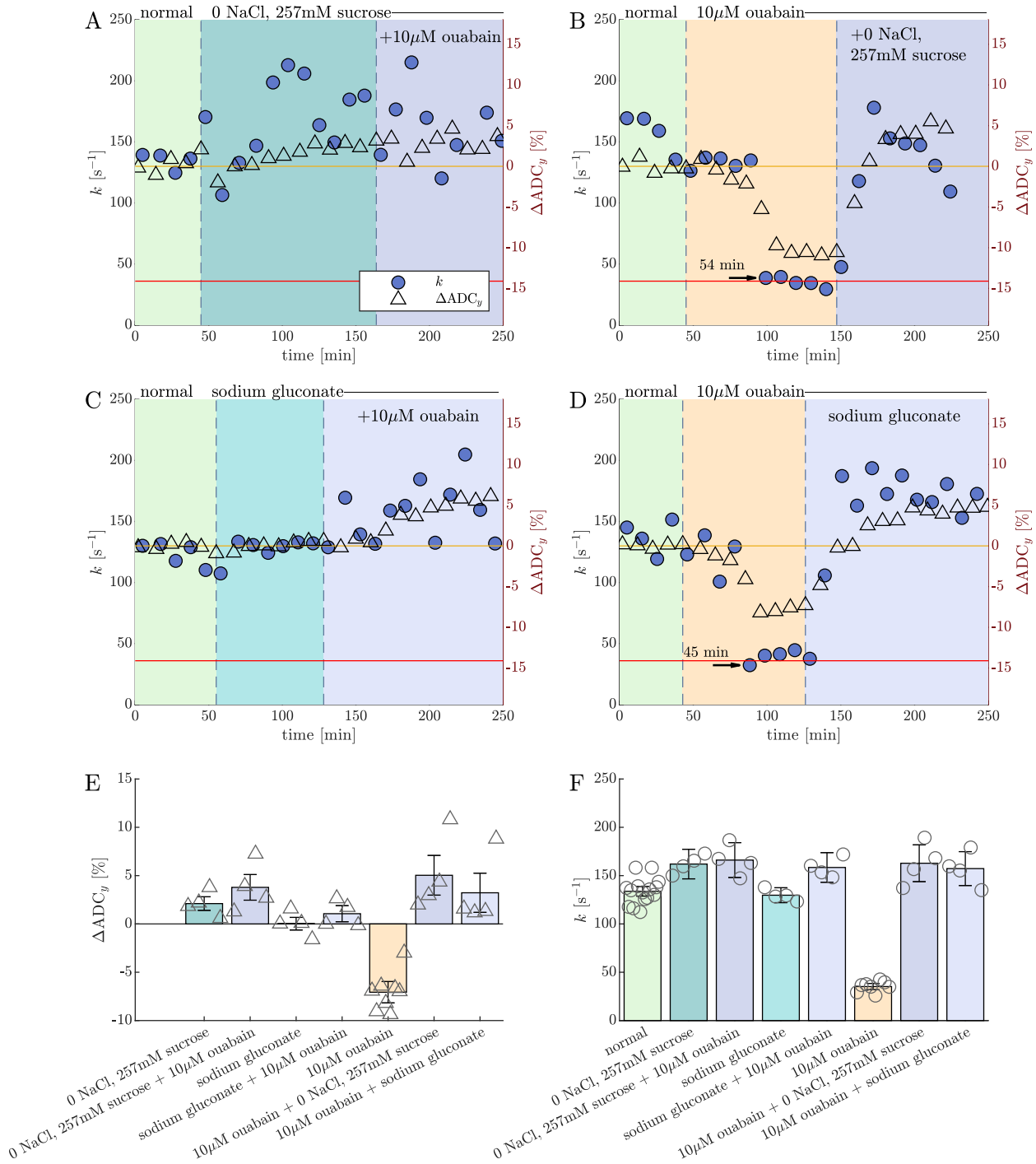

Fig. 2. Exchange rate is not directly linked to ion transport, voltage, or active water cycling. A–D) Representative recording of k (blue circles) and % change in ADC_y (open triangles) during experiments involving (A,C) washing the sample from normal media to media in which NaCl was replaced with equiosmolar concentration of (A) sucrose (257 mM) or (C) sodium gluconate (128 mM), and then adding 10 μM ouabain, and (B,D) adding 10 μM ouabain on top of normal medial, waiting for the effect, and then washing to (B) 0 NaCl, 257 mM sucrose media or (D) sodium gluconate media in the presence of 10 μM ouabain. E,F) Box plots of (E) $\Delta\mathrm{ADC}_y$ and (F) k under the various conditions.

between osmotic pressure π and osmolyte concentration c,

$$\pi = cRT \tag{2}$$

where R is the ideal gas constant and T is the absolute temperature.[56] This relationship is valid for the dilute sucrose concentrations we study here.[57] For reference, the Van't Hoff equation predicts $+100$ mOsm at 25°C (or 298.15°K) to increase osmotic pressure by $+240$ kPa.

First, the effect of 100 mOsm sucrose was observed on the same sample before and after adding 10 μM ouabain (Fig. 3). ADC_y followed trends expected for cellular shrinking and swelling; it increased in the 100 mOsm hypertonic conditions, recovered in normal isotonic media, and decreased slightly when ouabain took effect (Fig. 3 A and B). k followed similar trends, although osmolytes had a much larger effect after the sample was treated with ouabain (Fig. 3 C

and D). Starting from the normal condition, 100 mOsm increased k slightly but not significantly, by $14 \pm 25\%$. After ouabain took effect, 100 mOsm increased k much more, by $233 \pm 68\%$. k dropped back down when the osmolyte was washed away in the presence of ouabain (Fig. 3 C and D).

Next, effects of sucrose dosages in the range of 10 to 200 mOsm were studied on normal samples and on separate samples treated with 10 μM ouabain (Fig. 4 A and B). On normal samples, $\Delta\mathrm{ADC}_y$ and k increased only slightly; the effect was insignificant for dosages up to 100 mOsm but became significant at 200 mOsm (Fig. 4 C and E). For ouabain-treated samples, $\Delta\mathrm{ADC}_y$ and k increased significantly for doses between 30 mOsm and 100 mOsm. The trend changed at 200 mOsm, with $\Delta\mathrm{ADC}_y$ and k decreasing slightly, although not significantly (Fig. 4 C and E). Comparing $\Delta\mathrm{ADC}_y$ and k between the normal and ouabain-treated groups, both values were significantly lower for ouabain-treated samples at 0 mOsm and similar between groups at 100 mOsm. At 200 mOsm, k of ouabain-treated samples was significantly less than that of normal samples (Fig. 4 E) but $\Delta\mathrm{ADC}_y$ remained similar between sample groups (Fig. 4 C). The effects of mannitol were also studied on ouabain-treated samples (Fig. 4 D). Mannitol (MW= 182 g/mol) is a smaller molecule than sucrose (MW= 342 g/mol) and is also used as a cellular osmolyte.[19] Mannitol and sucrose increased $\Delta\mathrm{ADC}_y$ to similar values at each concentration (Fig. 4 C). This is in spite of sucrose reducing the ADC of pure aCSF media to a greater degree than mannitol due to its greater effect on fluid viscosity (Fig. S3). Thus the compounds' osmotic effects (cell shrinkage increasing ADC_y) are greater than their viscous effects (reducing ECS diffusivity). Their viscous effects may become apparent at higher concentrations, e.g. at 200 mM, where the average ADC of samples treated with sucrose is less than those treated with mannitol, although not significantly. Mannitol and sucrose also increased k similarly across concentrations (Fig. 4 E). This indicates that their effect on k is osmotic in nature.

We tested whether the effects of osmolytes were similar or different between normal and ouabain-treated groups by examining correlations between $\Delta\mathrm{ADC}_y$ and Δk (Fig. 4 F). The two groups have different correlations and occupy distinct regions of the plot (see distinct model fits and 95% CI). Data from normal samples appears clustered due to osmolytes having very little effect. For ouabain-treated samples, ADC_y and k show a sigmoidal relationship, being highly correlated at intermediate ADC_y and weakly correlated at low and high ADC_y. This behavior is not due to insensitivity to lower and higher exchange rates because we report lower exchange rates for ouabain-treated samples at 11°C (Fig. 5 E) and we previously reported higher exchange rates for normal samples at 35°C (in Fig. 1 B of Ref. 16). To completely recover k after ouabain treatment requires that ADC_y increase above baseline.

Osmotic perturbations with 100 mM sucrose and with variable concentrations up to 200 mM yielded consistent results overall (Fig. 4 C and E). Differences were observed during the wash from hypertonic media to normal media on samples not treated with ouabain. k recovered to stable values slightly below baseline after washing out the +100 mOsm solution, but dropped to low levels, similar to ouabain-treated values, after washing out the +200 mOsm solution. (compare Fig. 3 C to Fig. 4 A). It appears that the samples maintained homeostasis during the wash in the first case but not in the second. This could be because of the larger osmotic change in combination with a longer experiment time. Cells maintain volume under osmotic shock by regulatory volume decrease (RVD) mechanisms, which involve Na^+ and K^+ uptake coupled with electroneutral transport of $\mathrm{Cl}-$, in-part by reducing $\mathrm{Na}^+/\mathrm{K}^+$–ATPase activity.[55] 200 mM is more than the cells can physiologically balance given the limited NaCl and KCl in the aCSF and may have damaged the cells. Additionally, intracellular penetration of sucrose may have caused rebound swelling when washed to normal media. For reference, the wash occurred at roughly 120 minutes in the first case and at roughly 300 minutes in the second case.

Increasing extracellular tonicity reduces cell volume and likely also SVR. This alone will increase k (see Eq. 1). Activation energies measured from the temperature dependence of k can help determine whether extracellular osmolytes recover normal exchange rates after $\mathrm{Na}^+/\mathrm{K}^+$–ATPase inhibition by increasing SVR because, unlike rate constants, activation energies are independent of the membrane SVR.[31]

Tonicity affects activation energies of exchange but not of diffusion. The energy barriers of the various water exchange pathways can be probed by observing k at different temperatures. Here, we study samples under normal conditions, treated with 10 μM ouabain, treated with 100 mM sucrose, and treated with 10 μM ouabain and 100 mM sucrose. For each condition, k and ADC_y was recorded at 25°C and 11°C, and re-recorded at 25°C to test for sample recovery (Fig. 5 A–E). k recovered when re-recorded at 25°C (one-way ANOVA, $p > 0.05$). The dependence of k on the absolute temperature T is modeled with the Arrhenius equation

$$k = A\exp(-E_a/RT) \tag{3}$$

where A is the pre-exponential factor, E_a is the activation energy, and R is the ideal gas constant (Fig. 5 F). E_a values are similar between the normal samples ($E_a = 42.6 \pm 6.4\,\mathrm{kJ/mol}$) and normal $+100$ mOsm samples ($43.2 \pm 2.8\,\mathrm{kJ/mol}$), but different from the ouabain-treated samples ($25.2 \pm 0.8\,\mathrm{kJ/mol}$, Fig. 5 H). E_a recovers to $38.5 \pm 1.6\,\mathrm{kJ/mol}$ when $+100$ mOsm is added to ouabain-treated samples, indicating that the recovery is related to tonicity but not directly related to $\mathrm{Na}^+/\mathrm{K}^+$–ATPase activity. Since E_a values are independent of SVR, this also indicates that the major effect of tonicity on k is not through SVR changes. Faster k is associated with higher E_a (compare Fig. 5 E and H). This surprising result will be explained later.

Temperature affects water's thermal motion and self-diffusion coefficient. In tissue, the ADC depends on the diffusion length scale, which varies with temperature, leading to expected deviations from the E_a of pure water. Nonetheless, comparisons between conditions is still valid. In contrast to

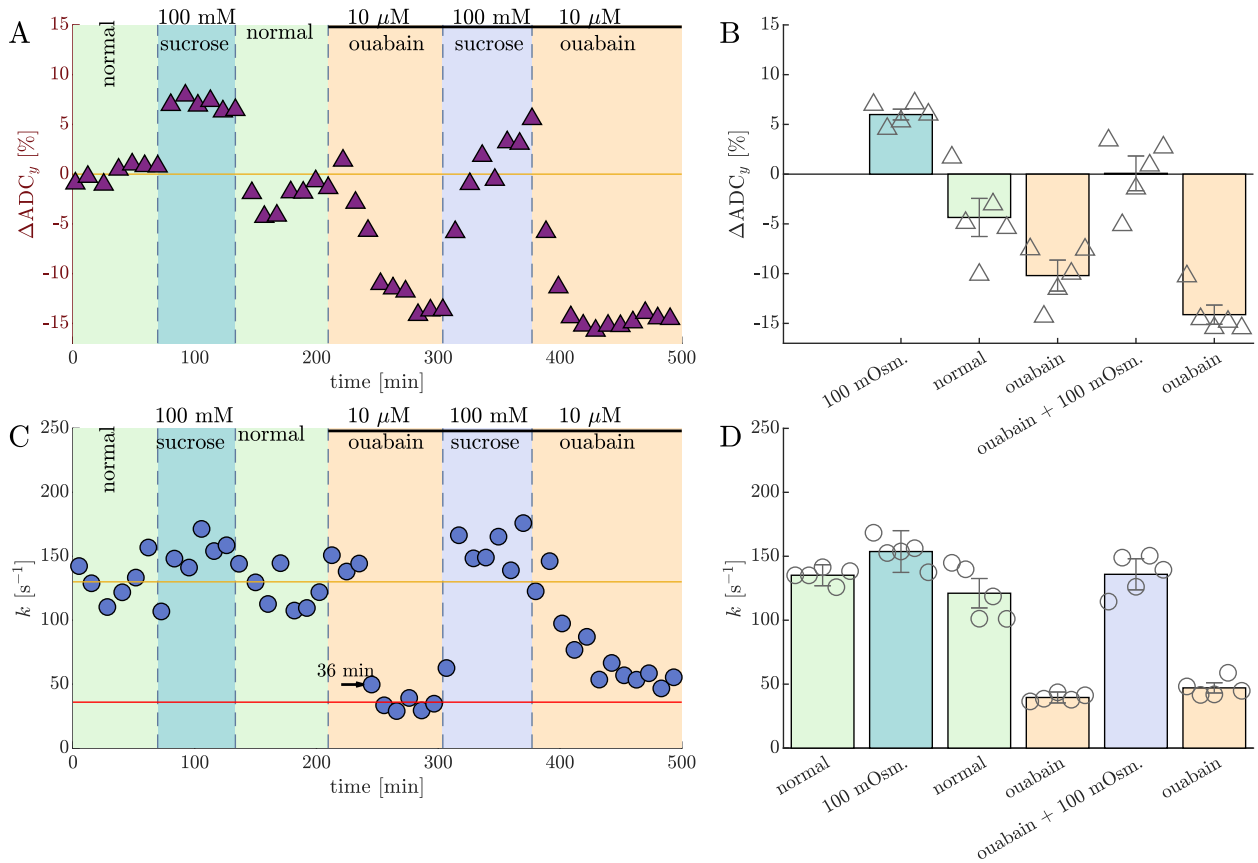

Fig. 3. Osmolytes recover exchange rate. A,C) Realtime measurements of (A) % change in ADC_y and (C) k during perturbations with 100 mM sucrose (an osmolyte) before and after the addition of 10 μM ouabain on a representative sample. The presence of 10 μM ouabain is shown by the solid-black line. B,D) Bar graphs showing the statistics across $n = 5$ samples.

k, the Arrhenius analysis of ADC_y yielded similar E_a values between conditions (Fig. 6). E_a values were lower than the value found for water self-diffusion in artificial cerebrospinal fluid (18 kJ/mol) likely due to water in the tissue experiencing more hindrances during the encoding time as its mobility increased with temperature.[16]

Exchange rate increasing with activation energy is explained by a multisite exchange mechanism. E_a and k increasing together is perhaps surprising. One might expect the opposite; a higher energy barrier should be associated with a slower transport rate. However, such behavior is commonly seen in heterogeneous systems when the overall rate depends on multiple competing processes with different activation energies[58] and when the relative contributions of these processes can be modulated by an additional component[59]. One signature of this behavior is a common linear dependence between E_a and the natural log of A across conditions

$$\ln(A) = m \times E_a + \ln(A'). \quad \textbf{(4)}$$

This is termed entropy–enthalpy compensation (EEC) because the activation energy E_a and the pre-exponential factor A are related to the enthalpy and entropy of the rate process, respectively.[58–63] EEC implies that the system under any condition can be described by a modified Arrhenius model of the form

$$k = A' \exp\left(-E_a/R\left(1/T - 1/T_c\right)\right) \quad \textbf{(5)}$$

with a common crossover temperature $T_c = 1/(m \times R)$ at which the rate constants are equal to A'.[60,63] Consistent with EEC, the E_a and $\ln(A)$ values were linearly related through Eq. 4 across all conditions (Fig. 7 A). This led to estimates of $T_c = -17°\mathrm{C}$ and $A' = 9.5\ \mathrm{s}^{-1}$ which, when put into Eq. 5, describes the temperature dependence of k for all systems (Fig. 7 B). Importantly, the EEC phenomena suggests a common mechanism exists under all conditions.[58] In this heterogeneous tissue the mechanism likely involves the modulation of multisite exchange pathways by tonicity. Consistent with this mechanism, we find that a three-site exchange model predicts the EEC behavior and a similar T_c and A' (Fig. 7 C and D). While samples could not be studied at temperatures down to T_c being that it is less than 0°C, simulations did show the exchange rates converging at T_c.

Discussion

Cells evolved semipermeable membranes to partition solutes while permitting water transport. These membranes enable cells to establish and control their electrochemical potential which is in turn used to maintain homeostasis and perform cellular functions. Part of ion and water homeostasis involves maintaining transmembrane isotonicity and regulating the volumes of intra- and extracellular spaces (ICS and ECS). Here we have demonstrated how the tonicity alone influences apparent steady-state water exchange. This tonicity depen-

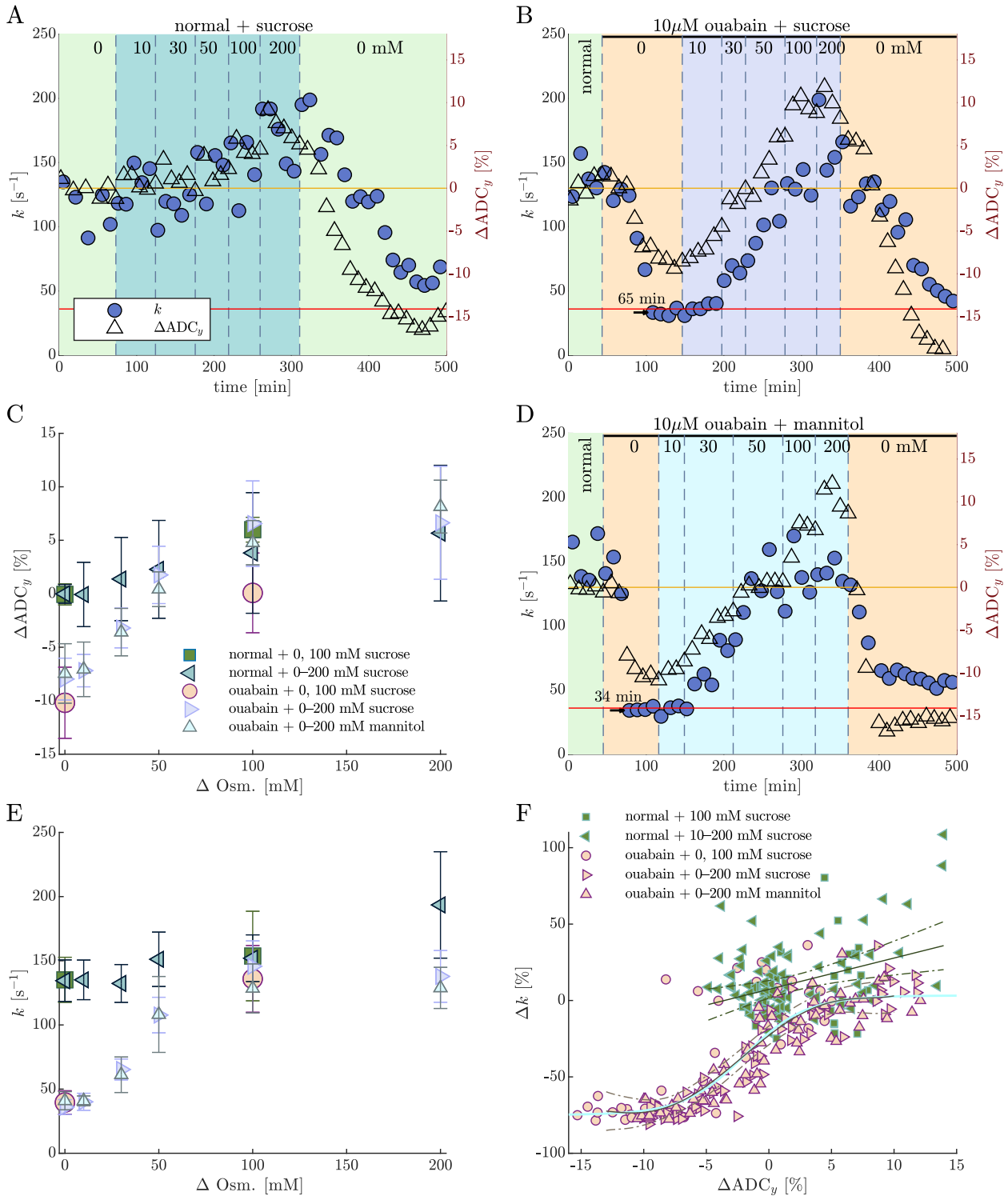

Fig. 4. Exchange rate depends on tonicity. A,B,D) Realtime measurements of k (left y-axis) and $\Delta\mathrm{ADC}_y$ (right y-axis) during osmotic perturbations with (A,B) sucrose or (D) mannitol concentrations 0, 10, 30, 50, 100, 200 mM and back to 0 mM on representative samples (A) starting from normal and (B,D) in the presence of 10 μM ouabain (shown by solid-back line). C,E) The effect of osmolarity on the mean (symbols) and standard deviations (error bars) of (C) ADC_y and (E) k when adding sucrose to samples under normal conditions ($n = 3$), and when adding sucrose ($n = 3$) or mannitol ($n = 3$) to samples treated with 10 μM ouabain (see legend in C). Data from Fig. 3 involving the addition of 100 mM sucrose in a single step pre-ouabain treatment and post-ouabain treatment are also shown. F) The correlation between $\Delta\mathrm{ADC}_y$ and Δk for all measurements performed on all samples in each group (see legend). Predicted means (solid lines) and 99% CI (broken lines) were found by regression of 1st order (combined normal samples) and 5th order (combined ouabain-treated samples) polynomials, with the latter being compared to a sigmoidal logistics function (aqua blue line).

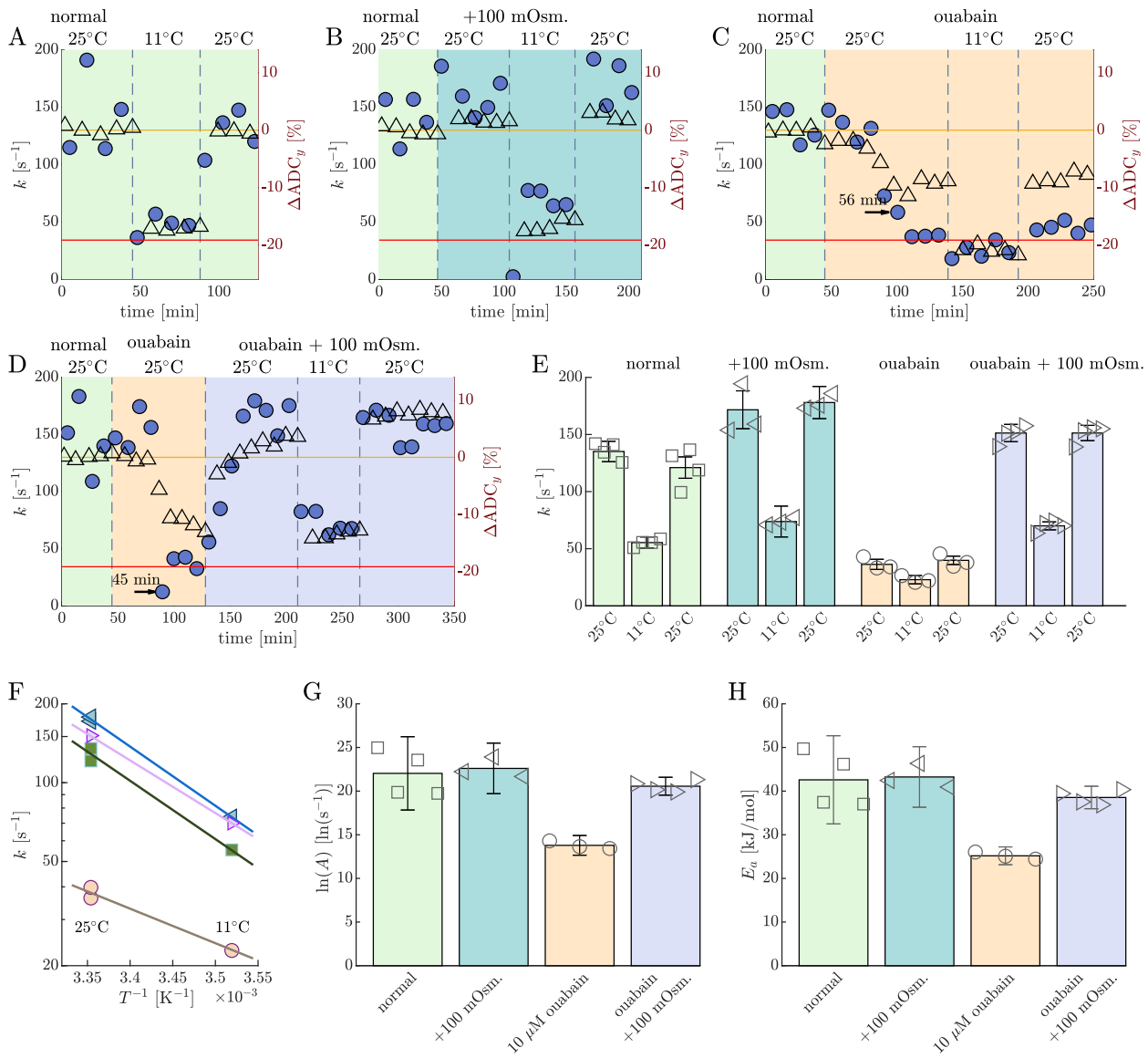

Fig. 5. Tonicity affects activation energies of exchange. A–D) Realtime measurement of k (blue circles) and $\Delta\mathrm{ADC}_y$ (open triangles) during temperature perturbation from 25°C to 11°C back to 25°C under (A) normal, (B) +100 mM sucrose, (C) 10 μM ouabain, (D) and 10 μM ouabain + 100 mM sucrose conditions. E) Results of k recorded at 25°C, 11°C, and again at 25°C on samples under normal ($n = 4$), + 100 mOsm ($n = 3$), 10 μM ouabain ($n = 3$), and 10 μM ouabain + 100 mOsm ($n = 4$) conditions. F) Arrhenius plot of the inverse of the absolute temperature T^{-1} vs. the average k for each condition. Solid lines show average fits of the Arrhenius model (Eq. 3). The slope of the line on the semi-log plot is proportional to E_a. G,H) Bar graph of (G) the natural log of pre-exponential factor A and (H) activation energy E_a estimated from Arrhenius model fits.

dence was observed regardless of the (non)equilibrium state of the tissue. It was seen when tonicity was established by the cells actively pumping and partitioning ions. It was also seen when tonicity was controlled by adding osmolytes while active ion transport was inhibited. This tonicity dependence does not involve water actively cycling with ions;[9–15] it was seen even when the majority of the ions were replaced by osmolytes. We found that passive water transport (i.e., diffusive permeability) can entirely explain how the exchange rate is (indirectly) related to cellular activity.

Spinal cords under various tonicity conditions showed Arrhenius behavior consistent with entropy–enthalpy compensation (EEC). EEC is commonly found in heterogeneous systems where the apparent rate constant involves multiple interconnected steps occurring in parallel or sequence and some factor modulates the appearance or dominance of certain steps.[58–63] In the spinal cord, EEC suggested the existence of multisite exchange, and that tonicity affects k by modulating the dominance of certain exchange pathways. The mechanism may involve aspects related to the heterogeneity of the tissue microstructure.

The neonatal mouse spinal cord consists mostly of gray matter and little myelinated white matter.[64,65] Gray matter microstructure is characterized by the presence of branching cellular processes with sub-micron radii, and cell bodies (soma) with radii ranging from a few microns to tens of microns.[66–68] Recently, Khateri *et al.* demonstrated with Monte Carlo (MC) simulations that in such a heterogeneous microstructure, DEXSY may not be uniquely sensitive to transmembrane exchange but may also depend on various types

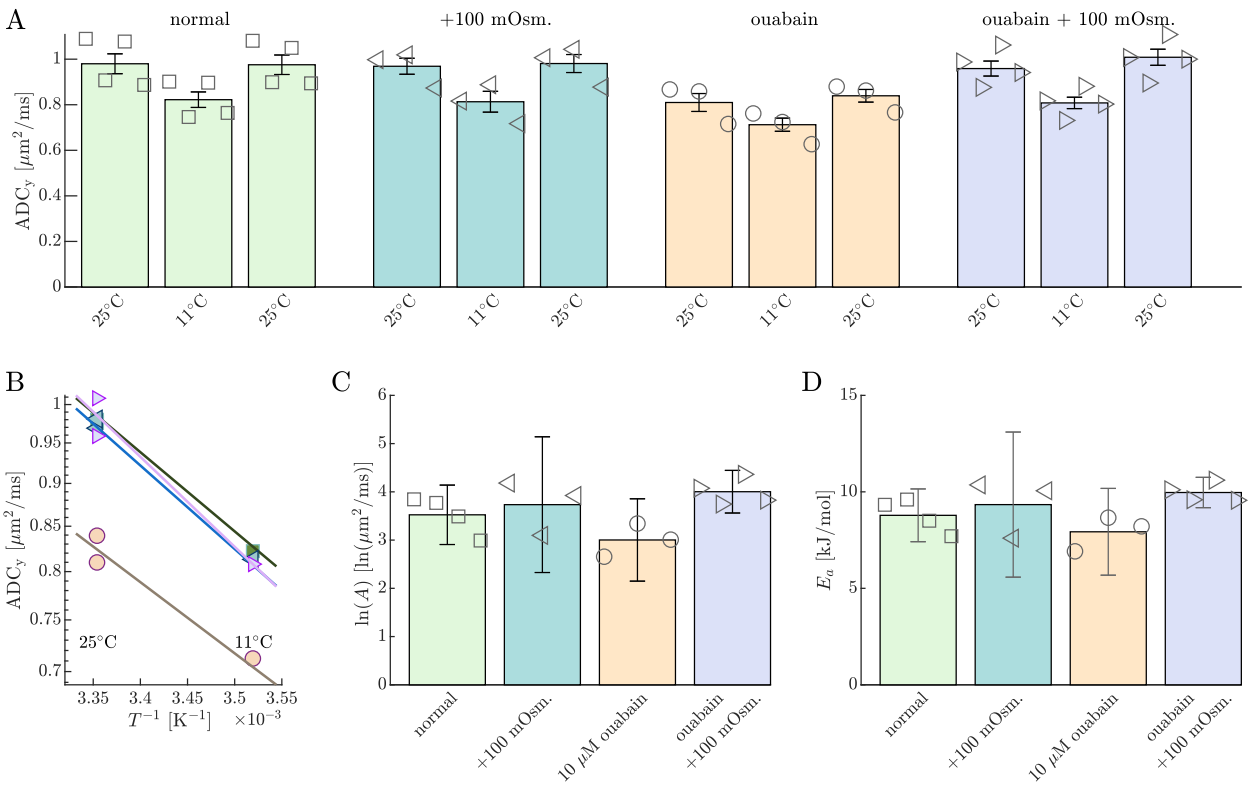

Fig. 6. Tonicity does not affect activation energies of diffusion. A) Results of $\mathrm{ADC_y}$ recorded at 25°C and 11°C and re-recorded at 25°C on samples under normal conditions ($n = 4$), after addition of 100 mM sucrose ($n = 3$), after the effect of 10 μM ouabain ($n = 3$), and after the combined effect of 10 μM ouabain and 100 mM sucrose ($n = 3$). B) Arrhenius plot of the inverse of the absolute temperature T^{-1} vs. the average $\mathrm{ADC_y}$ for each condition. Solid lines show average fits of the Arrhenius model (similar form to Eq. 3). C) Bar graph of the natural log of pre-exponential factor estimates. D) Bar graph of activation energy estimates.

of geometric exchange such as along branching processes.[7] This arises because DEXSY distinguishes exchange between compartments based on water translational mobility in the magnetic field gradient direction, not based on water's location in the ECS or ICS, *per se*. The distinguishing feature is the length scale of membranes surrounding the water relative to the dephasing length, $\ell_g = (D_0/\gamma g)^{1/3}$. ℓ_g is set by the gradient strength g and the self-diffusion coefficient D_0 and is here approximately 0.8 μm for water at 25°C.[30,69,70] Water within membrane structures with length scales similar or smaller than ℓ_g will appear less mobile than water in larger structures. Water diffusing within sub-micron processes running perpendicular to the gradient direction may appear less mobile on the timescale of diffusion encoding. Water diffusing in larger soma and in processes running parallel to the gradient direction may appear more mobile. Water in the ECS may also appear more mobile because it is a connected space, albeit a narrow and tortuous one. This motivated a three-site exchange model with exchange between a less mobile ICS compartment (**a**), a more mobile ICS compartment (**b**), and an ECS compartment (**c**), depicted in Fig. 8. Here, compartment mobility refers to the average mobility of water within the compartment on the timescale of encoding. We ignored that some portion of water in the soma and ECS could appear less mobile due to localization near membrane surfaces oriented perpendicular to the gradient direction.[70–74]

Diffusion exchange measurements are only sensitive to exchange between compartments with distinct water mobilities. Sensitivity increases as the compartment mobilities shift further apart. Sensitivity to exchange with a compartment also depends on the fraction of the sample volume taken up by that compartment. If there are multiple compartments exchanging with one another, sensitivity to exchange pathways involving a certain compartment will depend on the compartment's volume fraction and its mobility relative to the other compartments. In this three-site exchange model for gray matter (Fig. 8), the apparent k is most sensitive to transmembrane exchange between compartments **a** and **c** and to geometric exchange between compartments **a** and **b** because these compartment pairs have the most disparate mobilities. k is less sensitive to transmembrane exchange between compartments **b** and **c** because these compartments have similar mobilities. While the values of k and ADC and their correlation depend on compartment mobilities (compare Figs. S4, S5, and S6), the overall trends and the EEC behavior are the same (compare Figs. 7 C,D, S7 and S8). Under normal and hypertonic conditions when there is significant ECS, the faster transmembrane exchange pathway (**a**–**c**) dominates over the slower geometric exchange pathway (**a**–**b**). Hypotonicity shifts water from the ECS (**c**) to ICS (**a** and **b**). This leads to the measurement being less sensitive to transmembrane exchange (**a**–**c**) and more sensitive to geometric exchange (**a**–**b**). This model provides a possible explanation for how k could depend on tonicity.

Previous studies of transmembrane water exchange in cellular systems generally suggest an inverse relationship be-

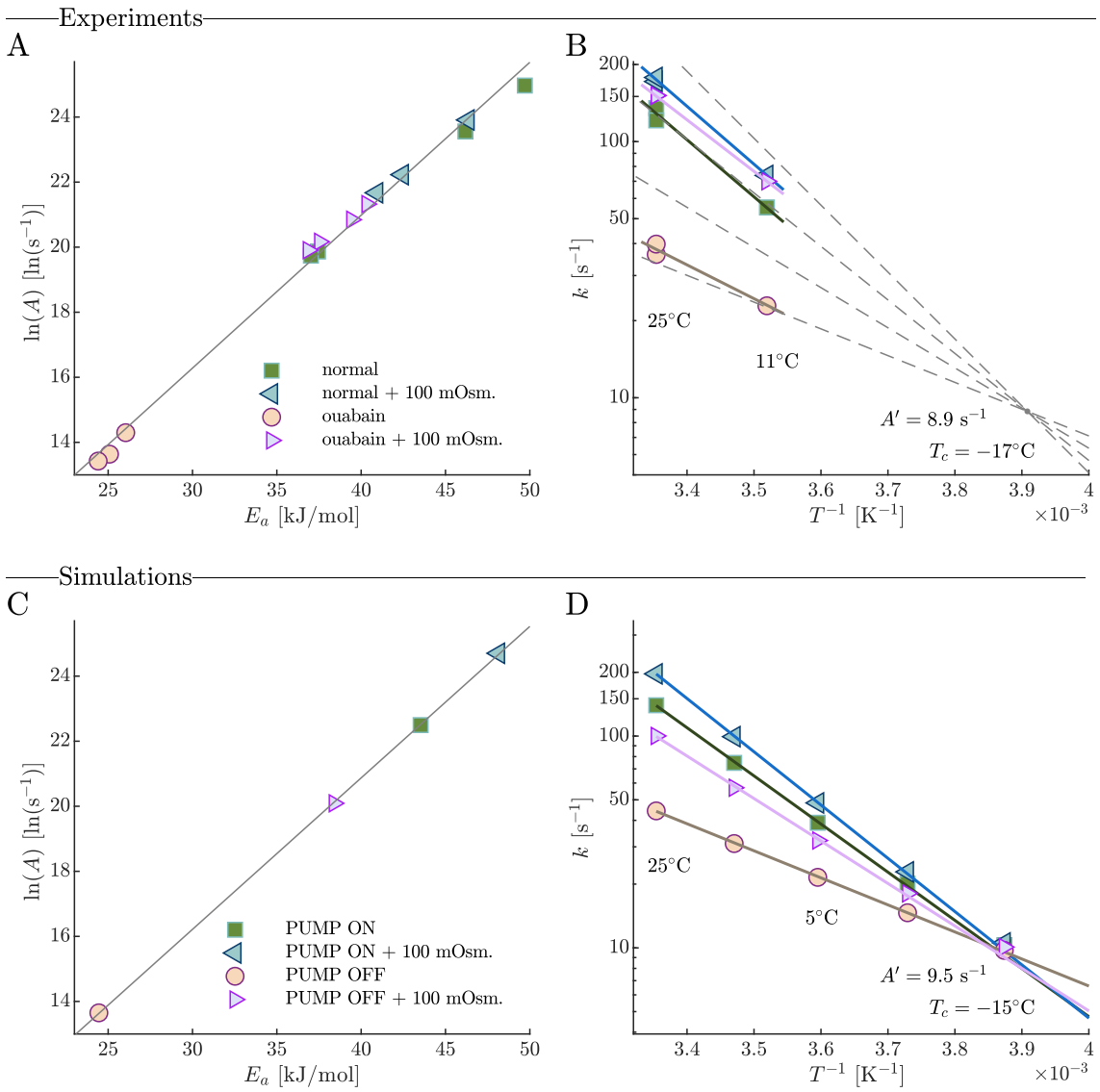

Fig. 7. Exchange rate increasing with activation energy is explained by a multisite exchange mechanism A) Experimental activation energies plotted vs. the natural log of pre-exponential factors for all samples show a linear dependence described by Eq. 4 with slope $m = 0.470\ \ln(\mathrm{s}^{-1})/(\mathrm{kJ/mol})$ (95% CI = 0.447, 0.493) and y-intercept $\ln(A') = 2.18\ \ln(\mathrm{s}^{-1})$ (95% CI =1.30, 3.06). This is a sign of entropy–enthalpy compensation and suggests a common crossover temperature $T_c = 1/(m \times R) - 273.15 = -17.1\ ^\circ$C (-29,-4.3). B) Semi-log plot of Eq. 5 for a range of E_a (dashed lines) along with the data from Fig. 5 F. C) E_a vs. $\ln(A)$ estimated from three-site model simulations. D) three-site model predictions of k at temperatures between -25 and $+25^\circ$C with the $\mathrm{Na}^+/\mathrm{K}^+$ PUMP ON or OFF and without or with the addition of 100 mOsm. (see legend in C). The modified Arrhenius model (Eq. 5) shows a common crossover temperature at $T_c = -15^\circ$C (-20,-9.2).

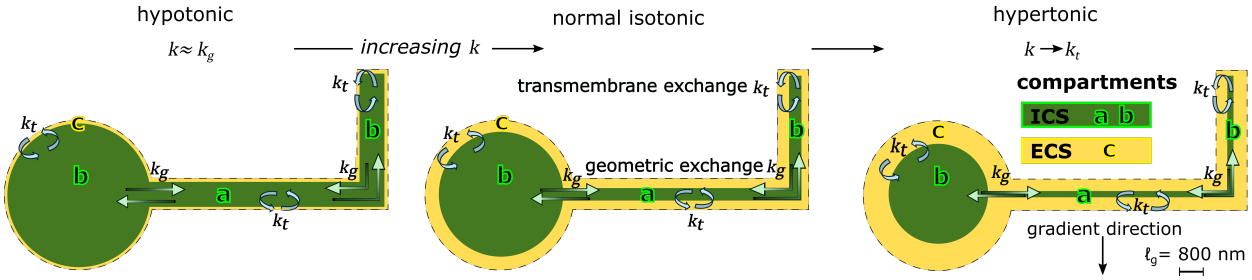

Fig. 8. Depiction of the connection between tonicity and k in a three-site model for gray matter. Compartment **a** represents cellular processes oriented perpendicular to the gradient direction. Compartment **b** represents cell bodies and processes oriented parallel to the gradient direction. Compartment **c** represents the ECS. Water in compartment **a** is less mobile in the gradient direction because the diameter of cellular processes is similar to or smaller than the dephasing length, ℓ_g. Water in compartments **b** and **c** is more mobile in the gradient direction because membrane length scales in that dimension are larger than ℓ_g. Transmembrane exchange k_t occurs between the ECS and ICS compartments: **a**–**c** and **b**–**c**. Geometric exchange k_g occurs between ICS compartments: **a**–**b**. In this model, tonicity modulates k by changing the fraction of ECS compartment **c** and the relative proportion of water seen exchanging with that compartment.

tween diffusive permeability (κ_d) and E_a. Cells devoid of water channels tend to have relatively lower κ_d and higher E_a because permeability depends on membrane fluidity which varies strongly with temperature.[31] For instance, $\kappa_d \approx 2\ \mu\mathrm{m/s}$ (at 25°C) and $E_a = 40\ \mathrm{kJ/mol}$ were found for Baker's Yeast in which permeability was low and presumed to be primarily across the lipid bilayer.[29] Aqueous channels across cell membranes such as aquaporins increase permeability and reduce E_a towards that of water self-diffusion ($E_a = 18-20\ \mathrm{kJ/mol}$)[75]. For instance, $\kappa_d \approx 40\ \mu\mathrm{m/s}$ (at 25°C) and $E_a \approx 25\ \mathrm{kJ/mol}$ were consistently reported for red blood cells[5] which have highly permeable plasma membranes due to high aquaporin expression.[76,77] In essence, the presence of water channels alters the dominant mechanism by which water crosses the membrane.

In contrast to the above trend, we found a positive relationship between k and E_a which trended with tonicity. The k (at 25°C) and E_a values for isotonic and hypertonic conditions (normal, normal + osmolyte, and ouabain-treated + osmolyte) were around 140–170 s^{-1} and 38–43 $\mathrm{kJ/mol}$ respectively. These values were significantly higher than found for the hypotonic condition (ouabain-treated) with k and E_a around 40 s^{-1} and 25 $\mathrm{kJ/mol}$ (Fig. 5 E and H). The trend is consistent with what we previously reported when comparing normal spinal cords ($140 \pm 16\ \mathrm{s}^{-1}$ and $36 \pm 7\ \mathrm{kJ/mol}$) to fixed spinal cords ($87 \pm 10\ \mathrm{s}^{-1}$ and $21 \pm 8\ \mathrm{kJ/mol}$).[16] Also consistent with this trend, Fritz and Swift (1967) found using a contrast agent-based NMR method to study water exchange in *ex vivo* frog sciatic nerves that $k = 6.8\ \mathrm{s}^{-1}$ and $E_a = 46\ \mathrm{kJ/mol}$ under normal conditions, but decreased below resolution after depolarization with either KCl or electrical stimulation.[8]

The positive relationship between k and E_a and their dependence on tonicity was explained by a multisite exchange mechanism and EEC (Fig. 7 A and B). The three-site model for gray matter (Fig. 8) was capable of predicting this behavior (Fig. 7 C and D). While not the only possible explanation, in this model the tonicity modulates the dominant pathways of apparent exchange between slower geometric exchange pathways and faster transmembrane exchange pathways by changing cell volume fraction.

The hypotonic (ouabain-treated) condition yielded E_a values similar to that of water self-diffusion.[75] This is consistent with geometric exchange involving self-diffusion though the aqueous ICS solution. Further, the exchange times for that condition (ouabain-treated $t_{ex} \approx k^{-1} \approx 25$ ms) were roughly consistent with MC simulation findings that soma–process exchange and exchange along branching processes in gray matter may become significant at times greater than 20 ms.[68,78]

The isotonic and hypertonic conditions yielded higher E_a values consistent with transmembrane exchange through the lipid bilayer. The high E_a indicates that aquaporin water channels are not a major exchange pathway. While perhaps a high E_a could result from active transport processes,[16] the E_a was also high when active transport was inhibited but tonicity was maintained (ouabain-treated + osmolyte condition). After eliminating transporters and channels, the only transmembrane exchange pathway which remains is the lipid bilayer.

It should be noted that varying the lipid bilayer composition can strongly affect its permeability.[20] Polyunsaturated lipids tend to increase permeability[20,79] whereas cholesterol tends to decrease permeability.[21] Plasma membranes in the CNS contain around 50% cholesterol and the remaining phospholipids are mostly unsaturated.[22] While reported permeability values can vary by over an order of magnitude between labs and techniques,[20,79] Huster *et al.* reported κ_d (at 25°C) between 70–400 $\mu\mathrm{m/s}$ and $E_a \approx 40\ \mathrm{kJ/mol}$ for a range of polyunsaturated lipid bilayers,[20] and Mathai *et al.* found 40% cholesterol to reduce permeability by 50%. Altogether this suggests that κ_d of some lipid bilayers in the CNS could be around 100 $\mu\mathrm{m/s}$. With the $\mathrm{SVR} \gtrsim 1\ \mu\mathrm{m}^{-1}$ for plasma membranes in gray matter,[19] Eq. 1 suggests that k values greater than 100 s^{-1} are conceivable.

Ouabain is considered a model for spreading depolarization[80] (or, more precisely, anoxic terminal spreading depolarization)[81] because it invokes the quintessential "all-or-none" nearly complete CNS cell depolarization.[82] Terminal spreading depolarization is accompanied by massive ion and water redistribution between ICS and ECS, hypotonicity, cell swelling, and dramatic ECS shrinkage.[46,47] The all-or-none drop of k and ADC_y we observed is likely a consequence of terminal spreading depolarization (Fig. 1). Similarities between the effect of ouabain on k in our study and its effect on membrane potential in Balestrino *et al.*[82] suggest that k and membrane potential may be linked. However, combined ouabain and sodium gluconate media perturbations indicated that k and membrane potential are only indirectly linked through the effect of membrane potential on tonicity (Fig. 2). The larger effect of ouabain on k relative to its effect on ADC_y can be explained by a multisite exchange model (Fig. S4), where k is related to the exchange rates between compartments and ADC is the weighted average over all compartments. These findings indicate that exchange rate measurements can be a biomarker for spreading depolarization, where the absolute value can distinguish the normal and depolarized states. For this purpose, show that k is more sensitive and specific than ADC measurements alone.[83] Results indicate that the mechanism involves the sensitivity of k to the hypotonic shift. The three-site exchange model further suggests that it is specifically measuring the dramatic ECS shrinkage during terminal spreading depolarization.

We found that the EEC model could describe the data under a range of tonicity conditions (Fig. 7). This suggests that there exists an EEC-based model to predict tonicity as a function of k. We follow Psurek *et al.* (2008) to derive a model for the enhancement of k at a tonicity (k_t) relative to a state of minimum (hypo)tonicity ($\theta = k_t/k_0$).[59] (See supplement for details.) After rearranging, the final result is

$$\Delta c = \ln(\theta)/\alpha, \tag{6}$$

where $\Delta c = c_t - c_0$ is defined as the change in effective osmolarity of solutes acting on the membrane, excluding the

contribution from naturally-occurring permanently trapped ECS and ICS impermeants. Additionnally,

$$\alpha = (\delta E_{at}/\Delta cRT) - (\delta S_t/\Delta cR), \quad \textbf{(7)}$$

where δE_{at} and δS_t are the enhancement of the activation energy and entropy by the tonicity at Δc. These can be expanded in a Taylor series about $\Delta c = 0$. To first order,

$$\alpha \approx [E_{at}]/T - [S_t], \quad \textbf{(8)}$$

where $[E_{at}]$ and $[S_t]$ are related to the first virial coefficients for the entropy and enthalpy of activation. While true only in the limit of $\Delta c \to 0$, the two parameters are calculated using $[E_{at}] = (E_{a(c=c_1)} - E_{a(c=c_0)})/(c_1 - c_0)R$ and $[S_t] = \ln(A_{c=c_1}/A_{c=c_0})/(c_1 - c_0)$ from measurements of E_a and A at $c = c_0$ and c_1.

For our system, by comparing E_a and A between the ouabain condition and the ouabain + 100 mOsm. condition, we find $[E_{at}] = 16.1$ °K/mM and $[S_t] = 0.0686$ mM^{-1}, leading to $\alpha \approx -0.0146$ mM^{-1} at 25°C. Based on k and k_0 from the normal and ouabain conditions respectively, we find $\theta = 130/35 = 3.7$, and Eq. 6 predicts $\Delta c = 90$ mOsm. This value is consistent with the osmolarity which recovered k of ouabain-treated samples back to normal values (130 s^{-1}), found to be 82 mOsm by fitting a linear model to k at sucrose concentrations between 0–100 mM for the ouabain-treated data in Fig. 4 E. The ability to quantify tonicity from exchange rate measurements could one day provide a quantitative biomarker of cell status.

Our MR hydrophysiology methods involved simultaneously collecting ADC_y and k. These metrics share a dependence on tonicity, but their values can not be predicted by changes in ECS volume fraction alone (compare correlation in Fig. 4 F to the three-site model prediction in Fig. S4 D). Their values do not always change together (i.e., they provide distinct information) because of inherent differences between the two measurements. Both measurements have the same ℓ_g and similar diffusion encoding times ($\tau \approx 0.5$ ms, corresponding to a diffusion length $\ell_d = \sqrt{\tau D_0} \approx 1$ μm at 25°C). Hence they similarly encode a blurred landscape of tissue compartments based on water's y-directional diffusive mobility on length scales around $\ell_g \approx 0.8$ μm. However, the exchange rate measurement probes a time window defined by the constant τ and variable mixing times ($\tau + t_m = 0.7$–300.5 ms corresponding to diffusion lengths ≈ 1.2–25 μm).[6] The ADC_y is averaged over all water compartments in the tissue. In contrast, the exchange rate is sensitive to water which appears to exchange between compartments with different mobility within the mixing time window. They provide different views of the heterogeneous tissue microstructure.

ADC_y and k do not always change together and therefore are not redundant measures because of various factors including differing sensitivities to pathway permeabilities, non-exchanging compartments, or water compartmental mobilities. Changes in pathway permeabilities will affect k more than ADC_y. Changes in the fraction or mobility of water which does not exchange within the mixing time window will affect ADC_y but not k. Changes in mobility of water in certain compartments will affect the ADC_y, but will also affect how sensitive k is to certain exchange pathways. It is also possible that the concept of compartments is over-simplified and effects like localization may need to be considered.[70–74] The strikingly sigmoidal relationship between ADC_y and k observed for ouabain-treated tissues at osmolarities from 0 to 200 mOsm indicates that tonicity affects these factors in a very repeatable way (Fig. 4 F).

Osmolytes were found to recover k without rescuing $\mathrm{Na}^+/\mathrm{K}^+$–ATPase activity. Hence k alone could not differentiate normal and ouabain-treated groups when osmolytes were also added. However, the combined information from $\Delta\mathrm{ADC}_y$ and Δk did separate the two states independent of the osmolarity (Fig. 4 F). This indicates that the added information includes some physiologically-regulated tissue properties. While the three site mechanism provides a starting point, it does not predict a difference in correlation between pump ON and OFF states (Figs. S4 D, S5 D, and S6 D). Future research should focus on understanding the shared and unique information provided by k and ADC and developing strategies to disentangle this information, especially when there is no baseline for calculating percent change, as is often the case clinically. One s

When normal tissue was treated with osmolytes, k stayed relatively constant whereas $\Delta\mathrm{ADC}_y$ varied more (see representative example in Fig. 3 A and C). k appears to be related to properties which are more tightly regulated, whereas $\Delta\mathrm{ADC}_y$ appears to be related to additional tissue properties which vary more during physiological perturbations. This is consistent with our previous findings of differing behavior between $\Delta\mathrm{ADC}_y$ and k during a stroke model involving insult and recovery from oxygen and glucose deprivation.[16] ADC_y was affected within 10 minutes of initiating OGD and 20 to 30 minutes before k was affected. ADC_y recovered when restoring oxygen and glucose while k remained suppressed (Fig. 4 of Ref. 16). In that study, it appeared that k was tightly regulated unitl homeostasis could no longer be maintained, at which point k dropped and did not recover. This led us to speculate that k was reflective of tissue viability. This could still be true, although under a different mechanism than a direct link to active transport as we previously thought.

Part of this mechanism may involve homeostatic regulation. Cells have mechanisms such as RVD for maintaining isotonicity under osmotic changes.[55] Most of these mechanisms utilize ionic gradients established by the $\mathrm{Na}^+/\mathrm{K}^+$–ATPase and are hence blocked by ouabain. The weak effect of osmolytes on ADC_y and k of normal samples compared to ouabain-treated samples, particularly at 50 mM concentrations and below, is consistent with the effect of RVD mechanisms (Fig. 4). The lack of effect seen when washing from aCSF to sodium gluconate media despite its higher effective osmolarity, and the increase in ADC and k when ouabain was added implicates (in this experiment) a subset of regulatory volume decrease mechanisms which can operate with only 7 mM $\mathrm{Cl}-$ present in the media (Fig. 2 C, E, and F). HCO^{3-}

could take the place of $\mathrm{Cl}-$ to maintain electroneutral transport of Na^+ and K^+.

The additional third compartment and second exchange pathway provided a minimal model for experimental observations which two-site exchange could not easily explain. In reality, however, the heterogeneity of gray matter tissue leads to many more than three tissue microenvironments. These microenvironments undergo microstructural changes during pathology, such as neurite beading,[84] affecting diffusion differently depending on the timescale.[85] Exchange processes may also deviate from first-order kinetics.[86] In view of this multicompartment tissue heterogeneity, we reiterate that the sensitivity to tissue compartments and exchange pathways is determined by the experimental parameters such as gradient strengths, durations, and timings.[69,70] This may explain why reported exchange rates and times for gray matter essentially span the entire range of NMR-accessible timescales.[11,13,16–18,30,87–98] Future efforts to model diffusion in gray matter should examine whether multisite exchange is important on the time and length scales of the MRI measurement, and what type of exchange (transmembrane or geometric) is being measured (if any). With the goal of developing and validating parsimonious biolphysical models of tisue microstructure and function, the added parameters of such a model calls for an even greater need to collect additional complementary information to characterize the tissue state. Promisingly, MR hydrophysiology pairs seamlessly with techniques like microscopy to gather complementary insights.[99]

Conclusion

Here we demonstrate that k depends on tonicity and not directly on activity. Entropy–enthalpy compensation suggests the mechanism involves multisite exchange. A three-site exchange model incorporating transmembrane and within-cell (geometric) pathways shows that the exchange rate can be modulated by the effect of tonicity on extracellular space volume. Transmembrane exchange across the plasma membranes of cell processes in CNS gray matter is fast $\gtrsim 100\ \mathrm{s}^{-1}$. Water channels and potential water cotransporters do not play a significant role in transmembrane exchange, suggesting that the primary pathway is through the lipid bilayer. In contrast, geometric exchange is slower $\approx 40\ \mathrm{s}^{-1}$. This may include exchange between soma and cell processes or along branching processes. Results suggest exchange rates can quantify tonicity and added information from ADC can help to differentiate normal tissue from inactive tissue under all tonicities. This motivates the translation of MR hydrophysiology methods to *in vivo* and suggests further possibilities for the use of combined water exchange and diffusion measurements as a proxy for homeostasis, tonicity, and overall tissue state during normal function, disease, development, aging and trauma.

ACKNOWLEDGEMENTS
NHW, RR, TXC, and PJB were supported by the IRP of the NICHD, NIH. We thank MJ O'Donovan and M Falgairolle for helpful discussions regarding the neonatal mouse spinal cord model, RW Pastor for input on lipid membrane permeability, and JF Douglas for bringing EEC to our attention.

CONTRIBUTIONS
Conceptualization, NHW, RR, TXC, JAR, and PJB; Methodology, NHW, RR, and TXC; Investigation, NHW and RR.; Writing – Original Draft, NHW; Writing – Review & Editing, NHW, RR, TXC, JAR, and PJB; Funding Acquisition, PJB; Supervision, PJB

DECLARATION OF INTERESTS
The authors declare no competing interests.

Bibliography

1. Marcus E Raichle. Two views of brain function. *Trends in cognitive sciences*, 14(4):180–190, 2010.
2. Fengfei Ding, John O'donnell, Qiwu Xu, Ning Kang, Nanna Goldman, and Maiken Nedergaard. Changes in the composition of brain interstitial ions control the sleep-wake cycle. *Science*, 352(6285):550–555, 2016.
3. Rune Rasmussen, John O'Donnell, Fengfei Ding, and Maiken Nedergaard. Interstitial ions: A key regulator of state-dependent neural activity? *Progress in neurobiology*, 193:101802, 2020.
4. Samo Lasič, Markus Nilsson, Jimmy Lätt, Freddy Ståhlberg, and Daniel Topgaard. Apparent exchange rate mapping with diffusion MRI. *Magnetic Resonance in Medicine*, 66(2):356–365, 2011.
5. Gheorghe Benga. Water transport in red blood cell membranes. *Progress in biophysics and molecular biology*, 51(3):193–245, 1988.
6. Teddy X Cai, Nathan H Williamson, Rea Ravin, and Peter J Basser. The diffusion exchange ratio (dexr): A minimal sampling of diffusion exchange spectroscopy to probe exchange, restriction, and time-dependence. *Journal of Magnetic Resonance*, page 107745, 2024.
7. Mohammad Khateri, Marco Reisert, Alejandra Sierra, Jussi Tohka, and Valerij G Kiselev. What does fexi measure? *NMR in Biomedicine*, 35(12):e4804, 2022.
8. OG Fritz Jr and TJ Swift. The state of water in polarized and depolarized frog nerves: A proton magnetic resonance study. *Biophysical Journal*, 7(6):675–687, 1967.
9. Charles S Springer Jr, Xin Li, Luminita A Tudorica, Karen Y Oh, Nicole Roy, Stephen Y-C Chui, Arpana M Naik, Megan L Holtorf, Aneela Afzal, William D Rooney, et al. Intratumor mapping of intracellular water lifetime: metabolic images of breast cancer? *NMR in Biomedicine*, 27(7):760–773, 2014.
10. William D Rooney, Xin Li, Manoj K Sammi, Dennis N Bourdette, Edward A Neuwelt, and Charles S Springer Jr. Mapping human brain capillary water lifetime: high-resolution metabolic neuroimaging. *NMR in Biomedicine*, 28(6):607–623, 2015.
11. Ruiliang Bai, Charles S Springer Jr, Dietmar Plenz, and Peter J Basser. Fast, na+/k+ pump driven, steady-state transcytolemmal water exchange in neuronal tissue: A study of rat brain cortical cultures. *Magnetic Resonance in Medicine*, 79(6):3207–3217, 2018.
12. Charles S Springer Jr. Using 1h2o mr to measure and map sodium pump activity in vivo. *Journal of Magnetic Resonance*, 291:110–126, 2018.
13. Ruiliang Bai, Charles S Springer Jr, Dietmar Plenz, and Peter J Basser. Brain active transmembrane water cycling measured by mr is associated with neuronal activity. *Magnetic resonance in medicine*, 81(2):1280–1295, 2019.
14. Charles S Springer Jr, Eric M Baker, Xin Li, Brendan Moloney, Martin M Pike, Gregory J Wilson, Valerie C Anderson, Manoj K Sammi, Mark G Garzotto, Ryan P Kopp, et al. Metabolic activity diffusion imaging [madi]: Ii. non-invasive, high-resolution human brain mapping of sodium pump flux and cell metrics. *NMR in Biomedicine*, page e4782, 2022.
15. Charles S Springer Jr, Eric M Baker, Xin Li, Brendan Moloney, Gregory J Wilson, Martin M Pike, Thomas M Barbara, William D Rooney, and Jeffrey H Maki. Metabolic activity diffusion imaging [madi]: I. metabolic, cytometric modeling and simulations. *NMR in Biomedicine*, page e4781, 2022.
16. Nathan H Williamson, Rea Ravin, Teddy X Cai, Melanie Falgairolle, Michael J O'Donovan, and Peter J Basser. Water exchange rates measure active transport and homeostasis in neural tissue. *PNAS nexus*, 2(3):pgad056, 2023.
17. Arthur Chakwizira, Ante Zhu, Thomas Foo, Carl-Fredrik Westin, Filip Szczepankiewicz, and Markus Nilsson. Diffusion mri with free gradient waveforms on a high-performance gradient system: Probing restriction and exchange in the human brain. *NeuroImage*, 283:120409, 2023.
18. Quentin Uhl, Tommaso Pavan, Malwina Molendowska, Derek K Jones, Marco Palombo, and Ileana Ozana Jelescu. Quantifying human gray matter microstructure using neurite exchange imaging (nexi) and 300 mt/m gradients. *Imaging Neuroscience*, 2:1–19, 2024.
19. Eva Syková and Charles Nicholson. Diffusion in brain extracellular space. *Physiological reviews*, 88(4):1277–1340, 2008.
20. Daniel Huster, Albert J Jin, Klaus Arnold, and Klaus Gawrisch. Water permeability of polyunsaturated lipid membranes measured by 17o nmr. *Biophysical journal*, 73(2):855–864, 1997.
21. John C Mathai, Stephanie Tristram-Nagle, John F Nagle, and Mark L Zeidel. Structural determinants of water permeability through the lipid membrane. *The Journal of general physiology*, 131(1):69–76, 2008.
22. Helgi I Ingólfsson, Timothy S Carpenter, Harsh Bhatia, Peer-Timo Bremer, Siewert J Marrink, and Felice C Lightstone. Computational lipidomics of the neuronal plasma membrane. *Biophysical journal*, 113(10):2271–2280, 2017.
23. P.T. Callaghan. *Translational Dynamics and Magnetic Resonance Principles of Pulsed Gradient Spin Echo NMR*. Oxford University Press, 2011.
24. John E Tanner. Transient diffusion in a system partitioned by permeable barriers. application to nmr measurements with a pulsed field gradient. *The Journal of Chemical Physics*, 69(4): 1748–1754, 1978.
25. Helene Benveniste, Laurence W Hedlund, and G Allan Johnson. Mechanism of detection of acute cerebral ischemia in rats by diffusion-weighted magnetic resonance microscopy. *Stroke*, 23(5):746–754, 1992.
26. David L Buckley, Jonathan D Bui, M Ian Phillips, Tibor Zelles, Benjamin A Inglis, H Daniel Plant, and Stephen J Blackband. The effect of ouabain on water diffusion in the rat

hippocampal slice measured by high resolution nmr imaging. *Magnetic Resonance in Medicine: An Official Journal of the International Society for Magnetic Resonance in Medicine*, 41(1):137–142, 1999.
27. Greg J Stanisz. Diffusion mr in biological systems: tissue compartments and exchange. *Israel journal of chemistry*, 43(1-2):33–44, 2003.
28. P. T. Callaghan and I. Furó. Diffusion-diffusion correlation and exchange as a signature for local order and dynamics. *The Journal of Chemical Physics*, 120(8):4032–4038, 2004.
29. Ingrid Åslund, Agnieszka Nowacka, Markus Nilsson, and Daniel Topgaard. Filter-exchange PGSE NMR determination of cell membrane permeability. *Journal of Magnetic Resonance*, 200(2):291 – 295, 2009. ISSN 1090-7807.
30. Nathan H Williamson, Rea Ravin, Dan Benjamini, Hellmut Merkle, Melanie Falgairolle, Michael James O'Donovan, Dvir Blivis, Dave Ide, Teddy X Cai, Nima S Ghorashi, et al. Magnetic resonance measurements of cellular and sub-cellular membrane structures in live and fixed neural tissue. *Elife*, 8:e51101, 2019.
31. AS Verkman. Water permeability measurement in living cells and complex tissues. *The Journal of membrane biology*, 173(2):73–87, 2000.
32. Yajie Zhang, Marie Poirier-Quinot, Charles S Springer Jr, and James A Balschi. Active trans-plasma membrane water cycling in yeast is revealed by nmr. *Biophysical journal*, 101 (11):2833–2842, 2011.
33. Donald DF Loo, Thomas Zeuthen, Grischa Chandy, and Ernest M Wright. Cotransport of water by the na+/glucose cotransporter. *Proceedings of the National Academy of Sciences*, 93(23):13367–13370, 1996.
34. AK Meinild, DA Klaerke, DDF Loo, EM Wright, and T Zeuthen. The human na+–glucose cotransporter is a molecular water pump. *The Journal of Physiology*, 508(Pt 1):15, 1998.
35. Thomas Zeuthen and Nanna MacAulay. Cotransporters as molecular water pumps. *International review of cytology*, 215:259–284, 2002.
36. Thomas Zeuthen. Water-transporting proteins. *Journal of Membrane Biology*, 234(2):57–73, 2010.
37. N MacAulay and T Zeuthen. Water transport between cns compartments: contributions of aquaporins and cotransporters. *Neuroscience*, 168(4):941–956, 2010.
38. Nathan H Williamson, Rea Ravin, Teddy X Cai, Dan Benjamini, Melanie Falgairolle, Michael J O'Donovan, and Peter J Basser. Real-time measurement of diffusion exchange rate in biological tissue. *Journal of Magnetic Resonance*, 317:106782, 2020.
39. G Eidmann, R Savelsberg, Peter Blümler, and Bernhard Blümich. The nmr mouse, a mobile universal surface explorer. *Journal of Magnetic Resonance*, 122:104–109, 1996.
40. D.G. Rata, F. Casanova, J. Perlo, D.E. Demco, and B. Blümich. Self-diffusion measurements by a mobile single-sided nmr sensor with improved magnetic field gradient. *Journal of Magnetic Resonance*, 180(2):229 – 235, 2006. ISSN 1090-7807. doi: https://doi.org/10.1016/j.jmr.2006.02.015.
41. Federico Casanova, Juan Perlo, and Bernhard Blümich. *Single-sided NMR*. Springer, 2011.
42. Erwin L Hahn. Spin echoes. *Physical review*, 80(4):580, 1950.
43. Teddy Xuke Cai. *In search of lost time: development of rapid magnetic resonance methods to probe time-varying diffusion*. PhD thesis, University of Oxford, 2023.
44. Alan R Kay. How cells can control their size by pumping ions. *Frontiers in cell and developmental biology*, 5:41, 2017.
45. Melanie Falgairolle, Joshua G Puhl, Avinash Pujala, Wenfang Liu, and Michael J O'Donovan. Motoneurons regulate the central pattern generator during drug-induced locomotor-like activity in the neonatal mouse. *Elife*, 6:e26622, 2017.
46. George G Somjen. Mechanisms of spreading depression and hypoxic spreading depression-like depolarization. *Physiological reviews*, 81(3):1065–1096, 2001.
47. Miroslava Anděrová, Šárka Kubinová, Tomáš Mazel, Alexandr Chvátal, Camilla Eliasson, Milos Pekny, and Eva Syková. Effect of elevated k+, hypotonic stress, and cortical spreading depression on astrocyte swelling in gfap-deficient mice. *Glia*, 35(3):189–203, 2001.
48. RD Dortch, RA Horch, and MD Does. Development, simulation, and validation of NMR relaxation-based exchange measurements. *The Journal of Chemical Physics*, 131(16): 164502, 2009.
49. Maxime Van Landeghem, Agnes Haber, Jean-Baptiste D'espinose De Lacaillerie, and Bernhard Blümich. Analysis of multisite 2d relaxation exchange nmr. *Concepts in Magnetic Resonance Part A*, 36(3):153–169, 2010.
50. Stefanie Eriksson, Karin Elbing, Olle Söderman, Karin Lindkvist-Petersson, Daniel Topgaard, and Samo Lasič. NMR quantification of diffusional exchange in cell suspensions with relaxation rate differences between intra and extracellular compartments. *PloS one*, 12 (5):e0177273, 2017.
51. Zhaoqing Li, Zhenfeng Pang, Juange Cheng, Yi-Cheng Hsu, Yi Sun, Evren Özarslan, and Ruiliang Bai. The direction-dependence of apparent water exchange rate in human white matter. *NeuroImage*, 247:118831, 2022.
52. William J Obrien, Jerry B Lingrel, and Earl T Wallick. Ouabain binding kinetics of the rat alpha two and alpha three isoforms of the sodium-potassium adenosine triphosphate. *Archives of Biochemistry and Biophysics*, 310(1):32–39, 1994.
53. Jonathan T Ting, Tanya L Daigle, Qian Chen, and Guoping Feng. Acute brain slice methods for adult and aging animals: application of targeted patch clamp analysis and optogenetics. *Patch-clamp methods and protocols*, pages 221–242, 2014.
54. Michael Müller and George G Somjen. Intrinsic optical signals in rat hippocampal slices during hypoxia-induced spreading depression-like depolarization. *Journal of neurophysiology*, 82(4):1818–1831, 1999.
55. Thomas J Jentsch. Vracs and other ion channels and transporters in the regulation of cell volume and beyond. *Nature Reviews Molecular Cell Biology*, 17(5):293, 2016.
56. J. H. van't Hoff. Die rolle osmotischen drucks in der analogie zwischen losungen und gasen. *Zeitschrift fur physikalische Chemie*, 1:481–508, 1887.
57. Alessandro Grattoni, Manuele Merlo, and Mauro Ferrari. Osmotic pressure beyond concentration restrictions. *The Journal of Physical Chemistry B*, 111(40):11770–11775, 2007.
58. Wendell Q Sun. Dielectric relaxation of water and water-plasticized biomolecules in relation to cellular water organization, cytoplasmic viscosity, and desiccation tolerance in recalcitrant seed tissues. *Plant Physiology*, 124(3):1203–1216, 2000.
59. Tatiana Psurek, Christopher L Soles, Kirt A Page, Marcus T Cicerone, and Jack F Douglas. Quantifying changes in the high-frequency dynamics of mixtures by dielectric spectroscopy. *The Journal of Physical Chemistry B*, 112(50):15980–15990, 2008.
60. D Daoukaki-Diamanti, P_ Pissis, and G Boudouris. Depolarization thermocurrents in frozen aqueous solutions of mono-and di-saccharides. *Chemical physics*, 91(2):315–325, 1984.
61. A Anopchenko, Tatiana Psurek, David VanderHart, Jack F Douglas, and Jan Obrzut. Dielectric study of the antiplasticization of trehalose by glycerol. *Physical Review E*, 74(3): 031501, 2006.
62. Hiroyuki Sugimoto, Tsunehisa Miki, Kozo Kanayama, and Misato Norimoto. Dielectric relaxation of water adsorbed on cellulose. *Journal of Non-Crystalline Solids*, 354(27):3220–3224, 2008.
63. Marcus T Cicerone and Jack F Douglas. β-relaxation governs protein stability in sugar-glass matrices. *Soft Matter*, 8(10):2983–2991, 2012.
64. Alex M Henry and John G Hohmann. High-resolution gene expression atlases for adult and developing mouse brain and spinal cord. *Mammalian genome*, 23(9-10):539–549, 2012.
65. Gulgun Sengul, Ralph B Puchalski, and Charles Watson. Cytoarchitecture of the spinal cord of the postnatal (p4) mouse. *The Anatomical Record: Advances in Integrative Anatomy and Evolutionary Biology*, 295(5):837–845, 2012.
66. Hui-Hsin Tsai, Huiliang Li, Luis C Fuentealba, Anna V Molofsky, Raquel Taveira-Marques, Helin Zhuang, April Tenney, Alice T Murnen, Stephen PJ Fancy, Florian Merkle, et al. Regional astrocyte allocation regulates cns synaptogenesis and repair. *Science*, 337(6092): 358–362, 2012.
67. Dvir Blivis, Melanie Falgairolle, and Michael J O'Donovan. Dye-coupling between neonatal spinal motoneurons and interneurons revealed by prolonged back-filling of a ventral root with a low molecular weight tracer in the mouse. *Scientific Reports*, 9(1):1–9, 2019.
68. Marco Palombo, Andrada Ianus, Michele Guerreri, Daniel Nunes, Daniel C Alexander, Noam Shemesh, and Hui Zhang. Sandi: a compartment-based model for non-invasive apparent soma and neurite imaging by diffusion mri. *Neuroimage*, 215:116835, 2020.
69. Teddy X Cai, Nathan H Williamson, Rea Ravin, and Peter J Basser. Disentangling the effects of restriction and exchange with diffusion exchange spectroscopy. *Frontiers in Physics*, page 223, 2022.
70. Nathan H Williamson, Velencia J Witherspoon, Teddy X Cai, Rea Ravin, Ferenc Horkay, and Peter J Basser. Low-field, high-gradient nmr shows diffusion contrast consistent with localization or motional averaging of water near surfaces. *Magnetic Resonance Letters*, 2023.
71. MD Hurlimann, KG Helmer, TM Deswiet, and PN Sen. Spin echoes in a constant gradient and in the presence of simple restriction. *Journal of Magnetic Resonance*, 113:260–264, 1995.
72. Nicolas Moutal, Kerstin Demberg, Denis S Grebenkov, and Tristan Anselm Kuder. Localization regime in diffusion nmr: theory and experiments. *Journal of Magnetic Resonance*, 305: 162–174, 2019.
73. Nicolas Moutal and Denis S Grebenkov. The localization regime in a nutshell. *Journal of Magnetic Resonance*, 320:106836, 2020.
74. Hong-Hsi Lee, Els Fieremans, Susie Y Huang, Qiyuan Tian, and Dmitry S Novikov. Localization regime of diffusion in human gray matter on a high-gradient mr system: Sensitivity to soma size. In *Proceedings of the 30th Annual Meeting of ISMRM, Virtual*, 2021.
75. R Mills. Self-diffusion in normal and heavy water in the range 1-45. deg. *The Journal of Physical Chemistry*, 77(5):685–688, 1973.
76. J Bernard Heymann, Peter Agre, and Andreas Engel. Progress on the structure and function of aquaporin 1. *Journal of structural biology*, 121(2):191–206, 1998.
77. Philip W Kuchel and Gheorghe Benga. Why does the mammalian red blood cell have aquaporins? *Biosystems*, 82(2):189–196, 2005.
78. Andrada Ianus, Daniel C Alexander, Hui Zhang, and Marco Palombo. Mapping complex cell morphology in the grey matter with double diffusion encoding mr: A simulation study. *Neuroimage*, 241:118424, 2021.
79. Richard M Venable, Andreas Kramer, and Richard W Pastor. Molecular dynamics simulations of membrane permeability. *Chemical reviews*, 119(9):5954–5997, 2019.
80. Trent A Basarsky, Steven N Duffy, R David Andrew, and Brian A MacVicar. Imaging spreading depression and associated intracellular calcium waves in brain slices. *Journal of Neuroscience*, 18(18):7189–7199, 1998.
81. R David Andrew, Jed A Hartings, Cenk Ayata, KC Brennan, Ken D Dawson-Scully, Eszter Farkas, Oscar Herreras, Sergei A Kirov, Michael Müller, Nikita Ollen-Bittle, et al. The critical role of spreading depolarizations in early brain injury: consensus and contention. *Neurocritical care*, 37(Suppl 1):83–101, 2022.
82. Maurizio Balestrino, Jacob Young, and Peter Aitken. Block of (na+, k+) atpase with ouabain induces spreading depression-like depolarization in hippocampal slices. *Brain research*, 838(1-2):37–44, 1999.
83. Lawrence L Latour, Yasuhiro Hasegawa, James E Formato, Marc Fisher, and Christopher H Sotak. Spreading waves of decreased diffusion coefficient lifter cortical stimulation in the rat brain. *Magnetic resonance in medicine*, 32(2):189–198, 1994.
84. Matthew D Budde and Joseph A Frank. Neurite beading is sufficient to decrease the apparent diffusion coefficient after ischemic stroke. *Proceedings of the National Academy of Sciences*, 107(32):14472–14477, 2010.
85. Corey Allan Baron, Mahesh Kate, Laura Gioia, Kenneth Butcher, Derek Emery, Matthew Budde, and Christian Beaulieu. Reduction of diffusion-weighted imaging contrast of acute ischemic stroke at short diffusion times. *Stroke*, 46(8):2136–2141, 2015.
86. Alfredo Ordinola, Evren Özarslan, Ruiliang Bai, and Magnus Herberthson. Limitations and generalizations of the first order kinetics reaction expression for modeling diffusion-driven exchange: Implications on nmr exchange measurements. *The Journal of Chemical Physics*, 160(8), 2024.
87. James D Quirk, G Larry Bretthorst, Timothy Q Duong, Avi Z Snyder, Charles S Springer Jr, Joseph JH Ackerman, and Jeffrey J Neil. Equilibrium water exchange between the intra- and extracellular spaces of mammalian brain. *Magnetic Resonance in Medicine: An Official Journal of the International Society for Magnetic Resonance in Medicine*, 50(3):493–499, 2003.
88. Markus Nilsson, Jimmy Lätt, Danielle van Westen, Sara Brockstedt, Samo Lasič, Freddy Ståhlberg, and Daniel Topgaard. Noninvasive mapping of water diffusional exchange in the human brain using filter-exchange imaging. *Magnetic Resonance in Medicine*, 69(6):

1572–1580, 2013.
89. Donghan M Yang, James E Huettner, G Larry Bretthorst, Jeffrey J Neil, Joel R Garbow, and Joseph JH Ackerman. Intracellular water preexchange lifetime in neurons and astrocytes. *Magnetic resonance in medicine*, 79(3):1616–1627, 2018.
90. Björn Lampinen, Filip Szczepankiewicz, Danielle van Westen, Elisabet Englund, Pia C Sundgren, Jimmy Lätt, Freddy Ståhlberg, and Markus Nilsson. Optimal experimental design for filter exchange imaging: Apparent exchange rate measurements in the healthy brain and in intracranial tumors. *Magnetic resonance in medicine*, 77(3):1104–1114, 2017.
91. Ruiliang Bai, Zhaoqing Li, Chaoliang Sun, Yi-Cheng Hsu, Hui Liang, and Peter Basser. Feasibility of filter-exchange imaging (fexi) in measuring different exchange processes in human brain. *NeuroImage*, page 117039, 2020.
92. Jelle Veraart, Daniel Nunes, Umesh Rudrapatna, Els Fieremans, Derek K Jones, Dmitry S Novikov, and Noam Shemesh. Noninvasive quantification of axon radii using diffusion mri. *Elife*, 9:e49855, 2020.
93. Hong-Hsi Lee, Antonios Papaioannou, Dmitry S Novikov, and Els Fieremans. In vivo observation and biophysical interpretation of time-dependent diffusion in human cortical gray matter. *Neuroimage*, 222:117054, 2020.
94. Jin Zhang, Gregory Lemberskiy, Linda Moy, Els Fieremans, Dmitry S Novikov, and Sungheon Gene Kim. Measurement of cellular-interstitial water exchange time in tumors based on diffusion-time-dependent diffusional kurtosis imaging. *NMR in Biomedicine*, 34 (6):e4496, 2021.
95. Ileana O Jelescu, Alexandre de Skowronski, Françoise Geffroy, Marco Palombo, and Dmitry S Novikov. Neurite exchange imaging (nexi): A minimal model of diffusion in gray matter with inter-compartment water exchange. *NeuroImage*, 256:119277, 2022.
96. Jonas L Olesen, Leif Østergaard, Noam Shemesh, and Sune N Jespersen. Diffusion time dependence, power-law scaling, and exchange in gray matter. *NeuroImage*, 251:118976, 2022.
97. Eloïse Mougel, Julien Valette, and Marco Palombo. Investigating exchange, structural disorder, and restriction in gray matter via water and metabolites diffusivity and kurtosis time-dependence. *Imaging Neuroscience*, 2:1–14, 2024.
98. Chenyang Li, Els Fieremans, Dmitry S Novikov, Yulin Ge, and Jiangyang Zhang. Measuring water exchange on a preclinical mri system using filter exchange and diffusion time dependent kurtosis imaging. *Magnetic Resonance in Medicine*, 2022.
99. Ruiliang Bai, Andreas Klaus, Tim Bellay, Craig Stewart, Sinisa Pajevic, Uri Nevo, Hellmut Merkle, Dietmar Plenz, and Peter J Basser. Simultaneous calcium fluorescence imaging and mr of ex vivo organotypic cortical cultures: a new test bed for functional mri. *NMR in Biomedicine*, 28(12):1726–1738, 2015.

Supplementary Note 1: Additional PLM and three-site model details

The pump–leak model (PLM) uses the finite difference method to approximate the fluxes of ions based on their governing differential equations for mass conservation. Na^+ and K^+ transport actively with a 3:2 stoichiometry. Na^+, K^+, and Cl^- transport passively based on their electrochemical potential. The net charge of the intracellular impermeants is $z = -1$. Water permeability is assumed to be much higher than ion permeability and is not modeled directly. Instead, the cell changes volume so that the intracellular osmolarity matches the extracellular osmolarity at the end of each timestep. Voltage is modeled based on the net charge of the intracellular ions and the (constant) capacitance of the membrane. Unless stated otherwise, simulation parameters were the same as in Kay (2017). Volumes and voltages were taken as the values obtained at the final timestep. This time was sufficiently long for systems to reach steady-state (if there existed a stable steady-state), as determined by volume and voltage not changing when total time was increased by a factor of 10.

A three-site exchange model associated with two ICS compartments (**a** and **b**) and an ECS compartment (**c**) was developed for predicting ECS fraction (f_o), ADC and k (see Fig. 8). An analytical equation for the steady-state ECS fraction (f_o) was developed based on an osmotic balance which includes the contribution of an uncharged, trapped ECS osmolyte (x_o);

$$f_o = 1 - \frac{(1-z)x_i}{w_{tot}(\pi - 2Cl_o \exp(FV/RT)) + x_o/f_o} \tag{S1}$$

where x_i is number of moles of intracellular impermeants, π is the concentration of small osmolytes in the ECS, Cl_o is the concentration of extracellular chloride, F is the Faraday constant, R is the ideal gas constant, and T is the absolute temperature. π and Cl_o are assumed equal to that of the bathing media. The ECS and ICS volumes sum to a fixed total volume, w_{tot}. This equation does not model ion flux and instead assumes a value for the voltage (V). We used -48 mV for PUMP ON conditions and -10 mV for the PUMP OFF conditions. First, w_{tot} was set using the PLM to find the steady-state cell volume predicted with the PUMP ON but $x_o = 0$ and $f_o = 0.3$. Then x_o was arbitrarily set to $1/50$th of the moles of intracellular impermeants x_i. This caused the ECS volume fraction to increase slightly with the PUMP ON. Then Eq. S1 was used to predict ECS fraction f_o and osmolarities of intracellular and extracellular impermeants at varying osmolarities for the PUMP ON and PUMP OFF conditions (see, e.g., Fig S4).

Eq. S1 was used to define the fraction of compartment **c** ($f_c = f_o$). For simplicity, the fractions of the two ICS compartments were set equal, $f_b = f_a = (1 - f_c)/2$. The ECS compartment and a more mobile ICS compartment were both given $\mathrm{ADC}_c = \mathrm{ADC}_b = 1\ \mathrm{ms}/\mu\mathrm{m}^2$. A less mobile ICS compartment was given $\mathrm{ADC}_a = 0.1\ \mathrm{ms}/\mu\mathrm{m}^2$. Varying ADC values of the compartments affected the overall ADC, the size of effects on ADC, and the correlation between ADC and k (Figs. S4, S5, and S6) but had little effect on overall interpretations. Importantly, it did not affect the EEC relationship (Figs. 7 C and D, S7, and S8). ADC was modeled as the sum of the ADCs of each compartment multiplied by their volume fraction, $\mathrm{ADC} = f_c\mathrm{ADC}_c + f_b\mathrm{ADC}_b + f_a\mathrm{ADC}_a$. k was modeled by simulating data from the DEXSY experiment and then fitting the exchange model to the data. DEXSY signals were modeled using an operator formalism $S = [1,1,1] * OD_2 * OE * OD_1 * S_0$, ignoring relaxation. This involved multiplication of matrix exponentials which used the function $\mathrm{expm}()$ in MATLAB 2024a. Here, the operators for the first and second diffusion encoding blocks were $OD_{1,2} = \mathrm{expm}(-b_{1,2} * D)$ with $D = [\mathrm{ADC}_c, \mathrm{ADC}_b, \mathrm{ADC}_a]' . * \mathrm{eye}(3)$, where $\mathrm{eye}(3)$ is a 3×3 identity matrix. Equilibrium magnetization was $S_0 = [f_c, f_b, f_a]'$. The exchange operator was $OE = \mathrm{expm}(-t_m K)$ with exchange matrix

$$K = \begin{bmatrix} (f_b + f_a)k_t & -f_c k_t & -f_c k_t \\ -f_b k_t & f_c k_t + f_a k_g & -f_b k_g \\ -f_a k_t & -f_a k_g & f_c k_t + f_b k_g \end{bmatrix}$$

The exchange matrix included transmembrane exchange (k_t) and geometric exchange (k_g) pathways. Exchange rates were determined by the Arrhenius model (Eq. 3) with $T = 298.15$ K or varied in the simulation, using $E_a = 52\ \mathrm{kJ/mol}$ and $\ln(A) = 26.62\ \mathrm{s}^{-1}$ for k_t and $E_a = 22\ \mathrm{kJ/mol}$ and $\ln(A) = 12.52\ \mathrm{s}^{-1}$ for k_g. $\ln(A)$ values were chosen for each E_a using Eq. 4 and the slope and intercept values presented in the caption of Fig. 7. Columns of the exchange matrix sum to zero, satisfying the detailed balance. Parameters (timings, gradient, b_1 and b_2 protocol, mixing times, etc.) were set based on values used experimentally. k values were estimated using the same analysis method described in the "NMR hardware, experimental protocol, and analysis methods" section.

Supplementary Note 2: Derivation of EEC-based model to predict tonicity

In this section we derive a model relating the exchange rate to tonicity. The model is based on an application of transition state theory to the dynamics of mixtures. We first define the the enhancement of exchange with tonicity relative to a state of minimum (hypo)tonicity as $\theta = k_t/k_0$. Within transition state theory, $\theta = \exp(-\delta G_t/RT)$ where $\delta G_t = |G_t - G_0|$ is the change in Gibbs free energy associated with the difference in osmolarity of impermeable solutes in the extracellular space which increase the tonicity (hence the subscript t). Changes in Gibbs free energy can be decomposed into enthalpic and entropic contributions by

its thermodynamic definition $\delta G_t = \delta E_{at} - T\delta S_t$. Then

$$\begin{aligned}\theta &= \exp\left(\frac{-(\delta E_{at} - T\delta S_t)}{RT}\right)\\ &= \exp\left(\frac{\delta S_t}{R} - \frac{-\delta E_{at}}{RT}\right)\\ &= \exp\left(\frac{\delta S_t}{R}\right)\exp\left(\frac{-\delta E_{at}}{RT}\right).\end{aligned} \tag{S2}$$

To become the Arrhenius model, we explicitly define the connections between the change in entropy and the preexponential factors $\exp(\delta S_t/R) = A_t/A_0$, and between the change in enthalpy and the activation energies $\delta E_{at} = E_{at} - E_{a0}$. Here, A_t and E_{at} are tonicity-dependent and A_0 and E_{a0} are evaluated when the system is at a a state of minimum (hypo)tonicity, defining $c = 0$. Then

$$\begin{aligned}\theta &= \frac{A_t}{A_0}\exp\left(\frac{-(E_{at} - E_{A0})}{RT}\right)\\ &= \frac{A_t}{A_0}\frac{\exp(-E_{at}/RT)}{\exp(-E_{a0}/RT)}\end{aligned} \tag{S3}$$

Now the effect of tonicity on exchange can be considered in terms of its separate effect on δE_{at} and δS_t.
The analytical functions for δE_{at} and δS_t with respect to the osmotic concentration can be obtained by Taylor expansions,

$$\begin{aligned}E_{at} &= E_{a0} + \left.\frac{dE_{at}}{dc}\right|_{\Delta c\to 0}\Delta c + O(\Delta c^2) + ...\\ S_t &= S_0 + \left.\frac{dS_t}{dc}\right|_{\Delta c\to 0}\Delta c + O(\Delta c^2) + ...\end{aligned} \tag{S4}$$

where $O(\Delta c^2) + ...$ refer to second- and higher-order terms and $|_{\Delta c\to 0}$ refers to the term being evaluated in the limit of $\Delta c \to 0$, i.e., $c_t \to c_0$. We limit ourselves to a first-order approximation so that a two-parameter model can be obtained, but with the downside that the model loses validity as Δc increases above dilute concentrations. We also drop the evaluated symbol for brevity (although still implied). Then

$$\begin{aligned}\delta E_{at} &\approx dE_{at}/dc\ \Delta c\\ \delta S_t &\approx dS_t/dc\ \Delta c.\end{aligned} \tag{S5}$$

These two parameters can be calculated from measurements of E_a and A at $c = c_0$ and c_1 with $\Delta c = c_1$ by using the relations $dE_{at}/dc = (E_{a(c=c_1)} - E_{a(c=c_0)})/\Delta c$ and $dS_t/dc = \ln(A_{c=c_1}/A_{c=c_0})R/\Delta c$. These are related to virial coefficients for the entropy and enthalpy of activation by $[E_{at}] = (dE_{at}/dc)/R$ and $[S_t] = (dS_t/dc)/R$. These definitions are combined with Eq. S2 to obtain the final relationship

$$\theta = \exp(-\alpha\Delta c) \tag{S6}$$

where

$$\begin{aligned}\alpha &= (\delta E_{at}/\Delta cRT) - (\delta S_t/\Delta cR)\\ &\approx (dE_{at}/dc)/RT - (dS_t/dc)/R\\ &\approx [E_{at}]/T - [S_t].\end{aligned} \tag{S7}$$

From this model, it is also possible to calculate the tonicity Δc as

$$\Delta c = \ln(\theta)/\alpha. \tag{S8}$$

For our system, by comparing E_a and A of samples after treatment with ouabain to samples after treatment with ouabain and 100 mM sucrose ($c = c_0$ and $c = c_1$, respectively), we find $[E_{at}] = 16.1$ K/mM and $[S_t] = 0.0686$ 1/mM, leading to $\alpha \approx -0.0146$ 1/mM at 25°C. Based on k_t under normal and k_0 from ouabain-treated conditions $\theta = 130/35$, and Eq. S8 predicts $\Delta c = 90$ mOsm.

Supplementary figures

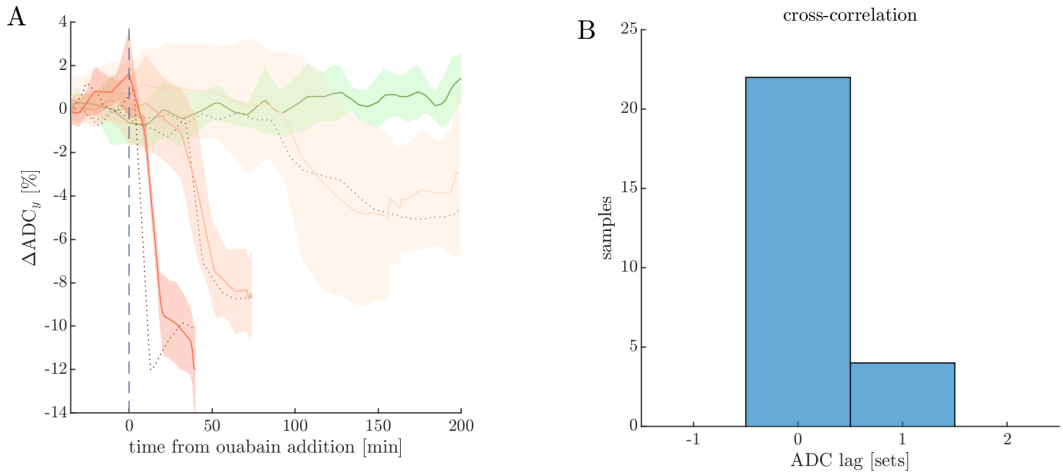

Fig. S1. ADC_y and k are affected by ouabain simultaneously. A) Mean (solid lines) and standard deviation (shaded regions) of realtime ADC_y measurements from a control group under normal conditions (green) and groups treated with 2, 10, and 100 $\mu\mathrm{M}$ ouabain (lightest to darkest colors) plotted against the time after addition of ouabain. Dotted lines show the mean of k for each group, scaled to the maximum and minimum of the mean of ADC_y for comparison. B) Histogram of the shift between the drop in ADC_y relative to the drop in k from a cross correlation analysis of 26 out of 28 samples for which there was a significant correlation between ADC_y and k ($cc > 0.2$, $p < 0.05$. Each set was 11 minutes to acquire and ADC_y measurements preceded k measurements. Analysis shows that ADC_y dropped either during the same set or the following set after k dropped, showing that ADC_y and k both dropped within 11 minutes of each other.

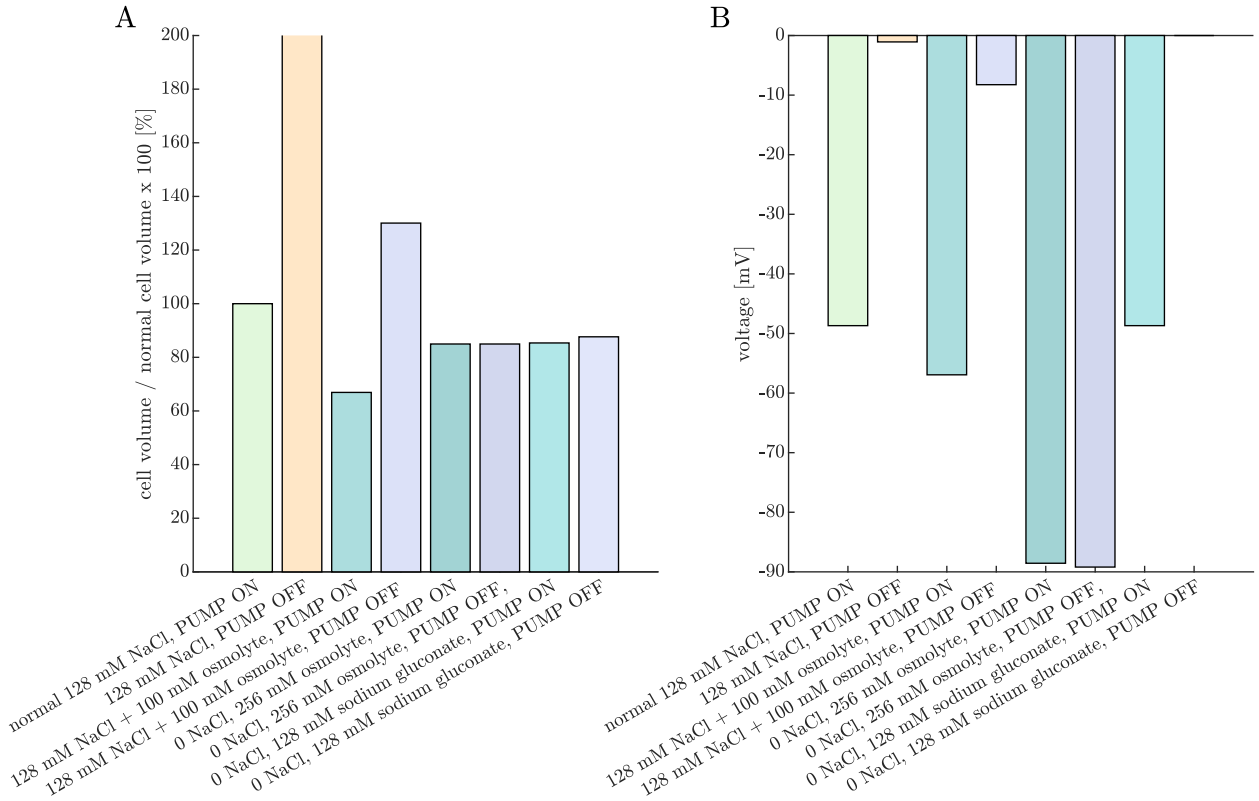

Fig. S2. Pump-leak model (PLM) provides predictions of cell volume and voltage under conditions studied experimentally. A) Percent change in cell volume and B) voltage predicted under various $\mathrm{Na^+/K^+ATPase}$ PUMP ON or OFF and media conditions after the PLM has run to steady-state (if applicable). With the 128 mM NaCl (and 4 mM KCl) media and PUMP OFF condition, the cell continues to swell and does not reach a steady-state. Addition of an osmolyte (+100 mOsm) reduces the volume and hyperpolarizes the cell in the PUMP ON condition, and stabilizes the volume but does not recover the voltage with the PUMP OFF. The cell volume is reduced to a similar level in both the PUMP ON and PUMP OFF conditions when NaCl is replaced by either sucrose or sodium gluconate (modeled as uncharged and monovalent anionic impermeants in the bathing media, respectively). However, while voltage is similar between the PUMP ON and PUMP OFF conditions when NaCl is replaced by sucrose, full depolarization to $\mathrm{V} = 0$ is predicted in the PUMP OFF condition with NaCl replaced by sodium gluconate.

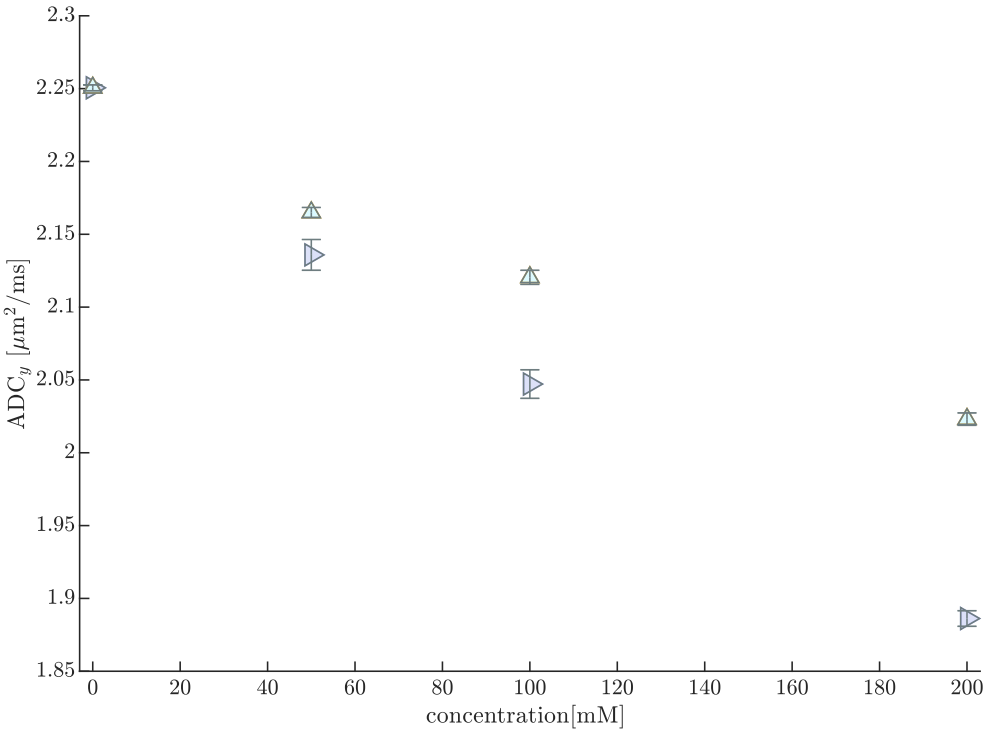

Fig. S3. Concentration-dependent effects of sucrose and mannitol on ADC of pure aCSF. Spin echo diffusion measurements were performed on aCSF at varying concentrations of sucrose (pink rightward-pointing triangles) or mannitol (aqua upward-pointing triangles) at 25°C without media circulation. At least three measurements were performed at each concentration using 8 τ values spaced linearly from $\tau = 105$ to $435\mu\mathrm{s}$ ($b = 0.0129$ to $0.9159\mathrm{ms}/\mu\mathrm{m}^2$), TR=2 s, and 2000 echoes. all other parameters were the same as standard diffusion measurements performed on spinal cords. Sucrose affects diffusion of water more than mannitol because it is a larger molecule (increased obstruction) and affects viscosity more (increased hydrodynamic interactions).

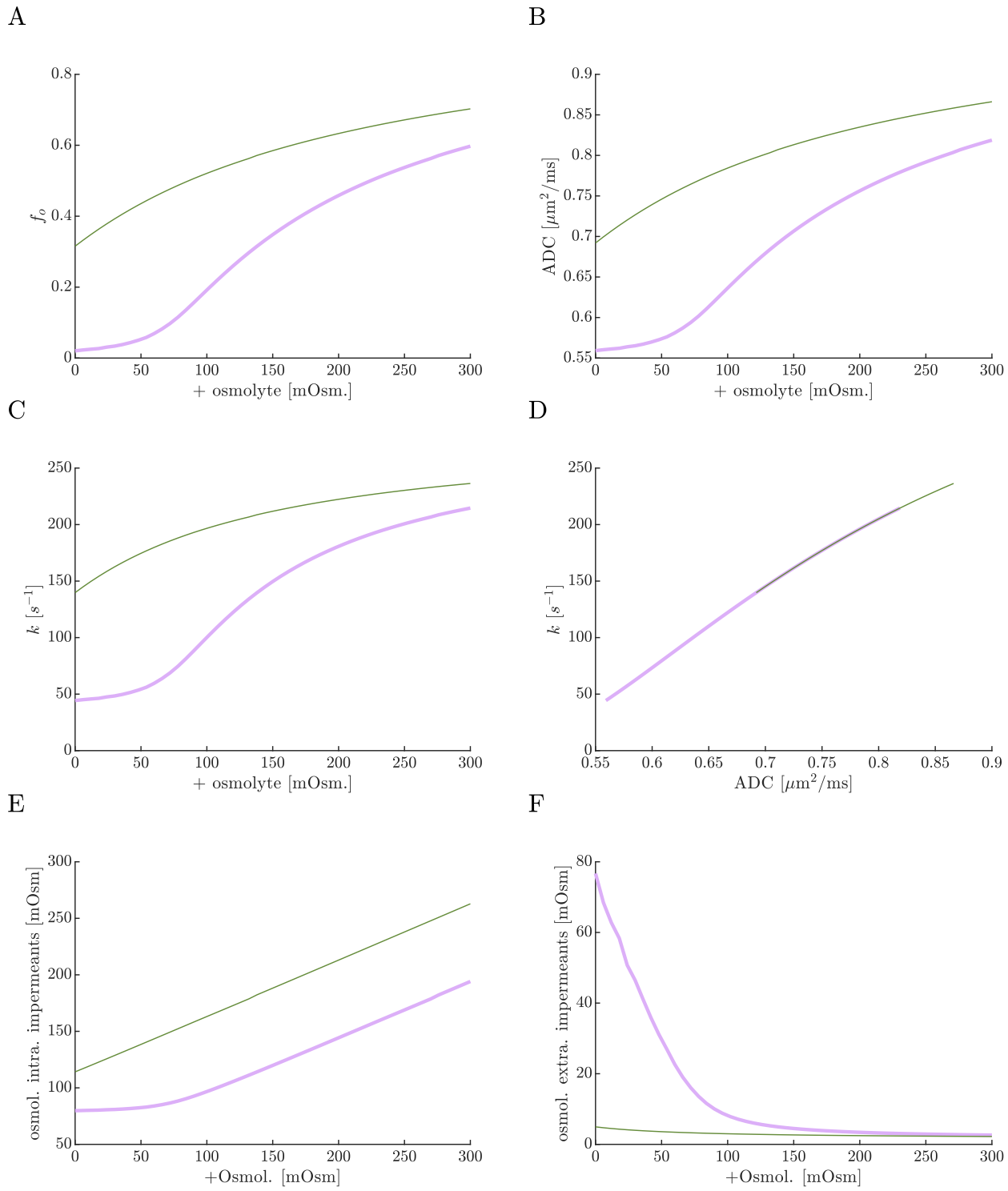

Fig. S4. Three-site model predicts ADC and k are affected by tonicity through a dependence on extracellular volume fraction. A) ECS volume fraction (f_o), B) ADC, C) k, D) the correlation between ADC and k, E) the osmolarity of intracellular impermeants, and F) the osmolarity of extracellular impermeants predicted using a 3-compartment model and three-site exchange model when an osmolyte is added to the normal media with $\mathrm{Na^+/K^+ATPase}$ ON (thinner green lines) and OFF (thicker pink lines). In this model, $\mathrm{ADC_a} = 0.1$, $\mathrm{ADC_b} = 1$, and $\mathrm{ADC_c} = 1\ \mathrm{ms}/\mu\mathrm{m}^2$, which are the same parameters used in Fig. 7 C,D.

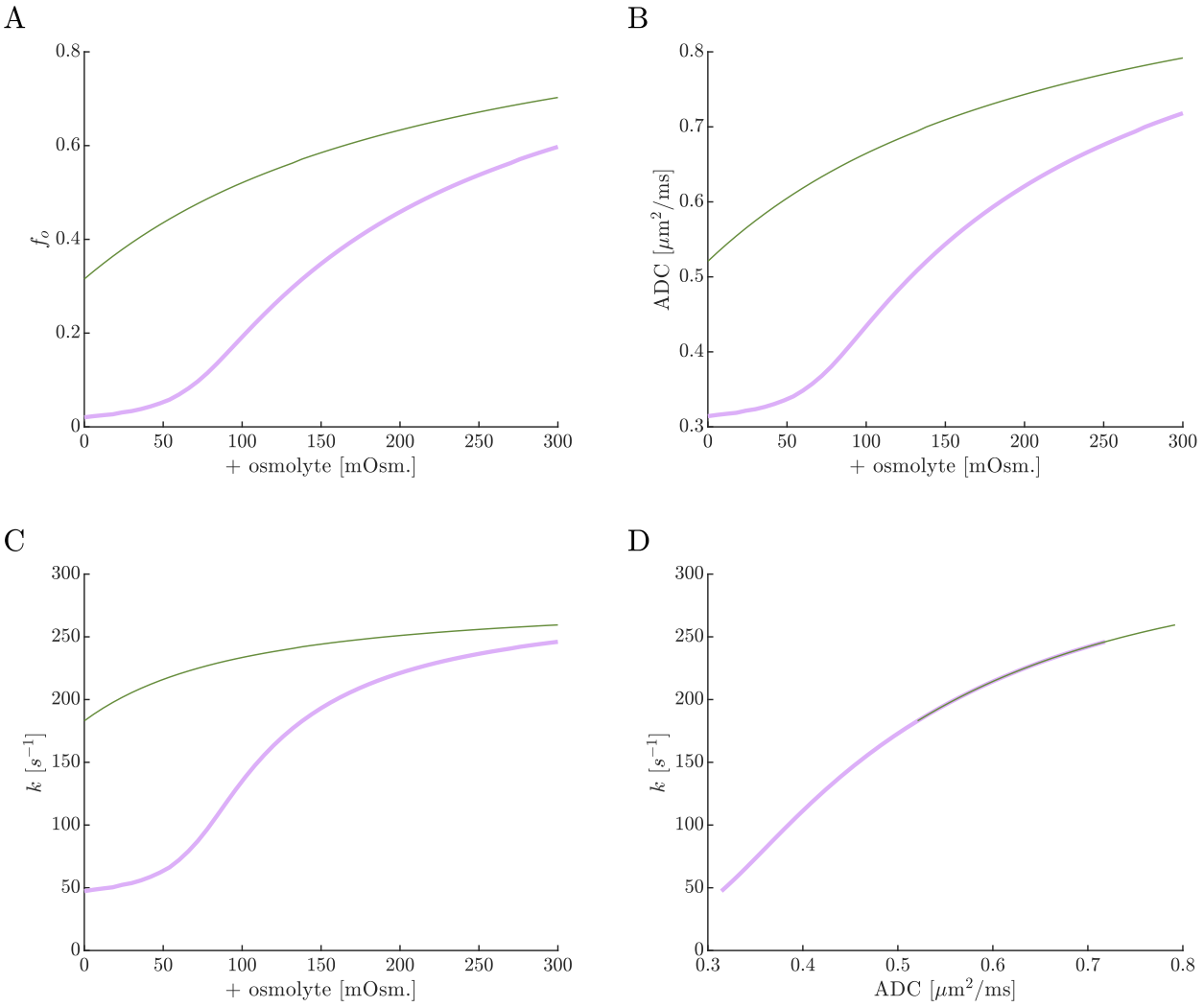

Fig. S5. Three-site model ADC and k estimates depend on compartment mobilities. A) ECS volume fraction (f_o), B) ADC, C) k, and D) the correlation between ADC and k predicted using a 3-compartment model and three-site exchange model when an osmolyte is added to the normal media with $\mathrm{Na^+/K^+ATPase}$ ON (thinner green lines) and OFF (thicker pink lines). In this model, $\mathrm{ADC_a} = 0.1$, $\mathrm{ADC_b} = 0.5$, and $\mathrm{ADC_c} = 1\ \mathrm{ms}/\mu\mathrm{m}^2$. The same parameters are also used in Fig. S7. f_o and the osmolarities of intracellular and extracellular impermeants are the same as in Fig. S4.

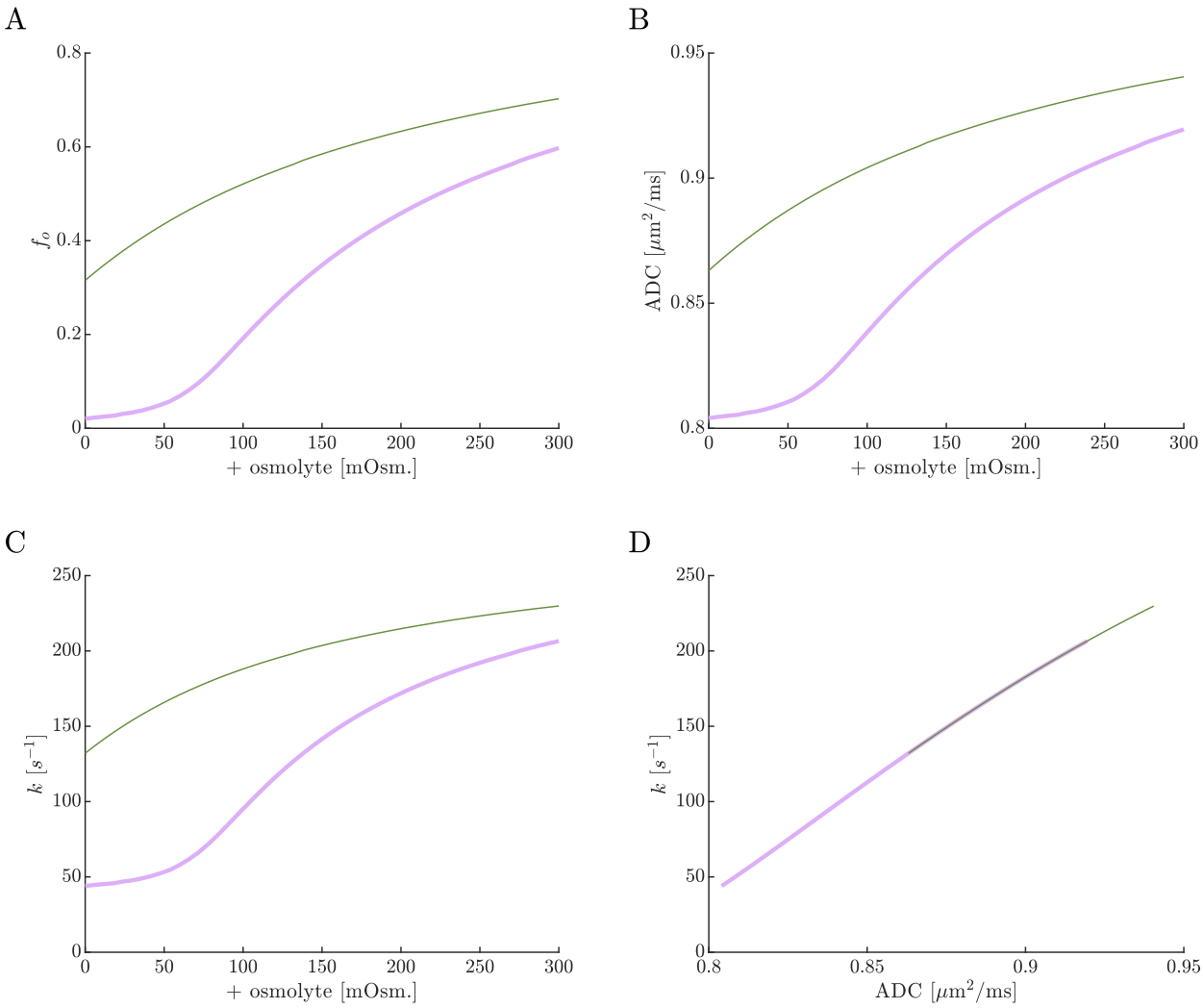

Fig. S6. Three-site model ADC and k estimates depend on compartment mobilities. A) ECS volume fraction (f_o), B) ADC, C) k, and D) the correlation between ADC and k predicted using a 3-compartment model and three-site exchange model when an osmolyte is added to the normal media with $\mathrm{Na}^+/\mathrm{K}^+\mathrm{ATPase}$ ON (thinner green lines) and OFF (thicker pink lines). In this model, $\mathrm{ADC_a} = 0.1$, $\mathrm{ADC_b} = 1.5$, and $\mathrm{ADC_c} = 1\ \mathrm{ms}/\mu\mathrm{m}^2$. The same parameters are also used in Fig. S8. f_o and the osmolarities of intracellular and extracellular impermeants are the same as in Fig. S4.

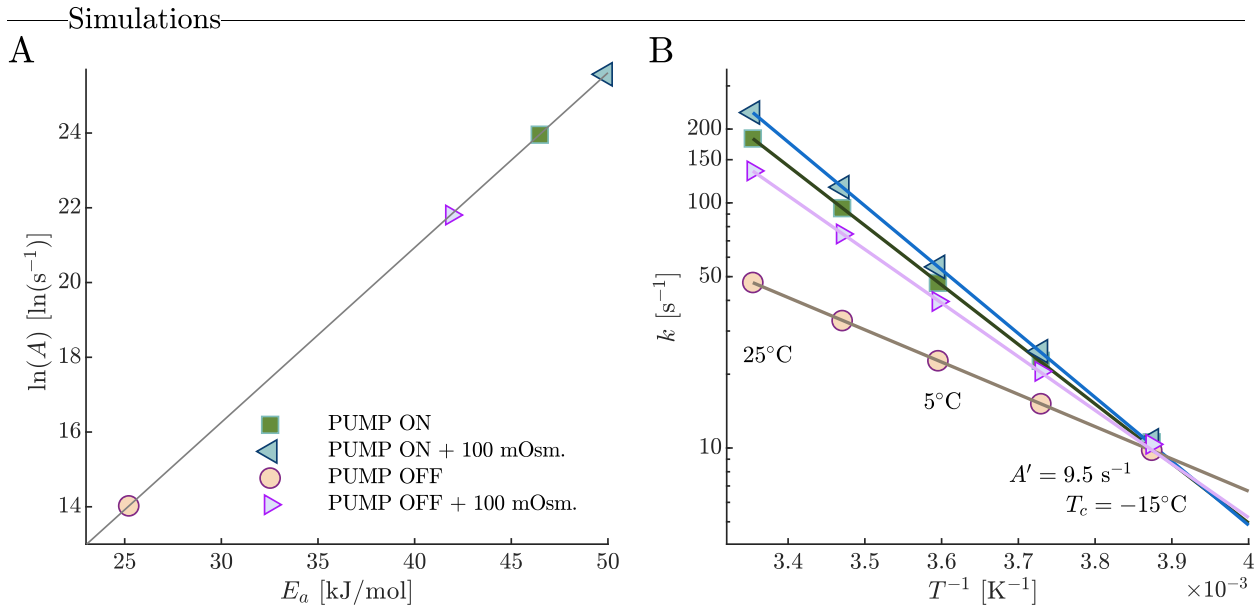

Fig. S7. EEC behavior does not depend on compartment mobilities in three-site model. A) E_a vs. $\ln(A)$ estimated from three-site model simulations. B) three-site model predictions of k at temperatures between -25 and $+25°$C with the Na^+/K^+ PUMP ON or OFF and without or with the addition of 100 mOsm. In this model, $\mathrm{ADC_a} = 0.1$, $\mathrm{ADC_b} = 0.5$, and $\mathrm{ADC_c} = 1\ \mathrm{ms}/\mu\mathrm{m}^2$. Note the similarity to Fig. 7 C,D, and Fig. S8 where compartment mobilities were different.

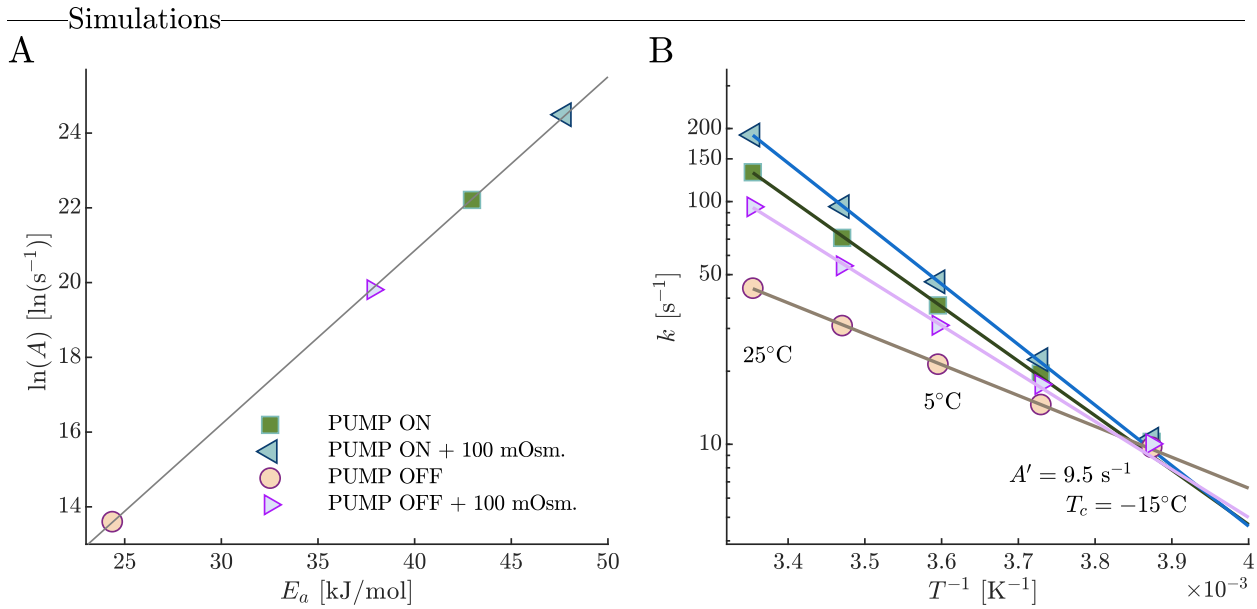

Fig. S8. EEC behavior does not depend on compartment mobilities in three-site model. A) E_a vs. $\ln(A)$ estimated from three-site model simulations. B) three-site model predictions of k at temperatures between -25 and $+25°$C with the Na^+/K^+ PUMP ON or OFF and without or with the addition of 100 mOsm. In this model, $\mathrm{ADC_a} = 0.1$, $\mathrm{ADC_b} = 1.5$, and $\mathrm{ADC_c} = 1\ \mathrm{ms}/\mu\mathrm{m}^2$. Note the similarity to Fig. 7 C,D, and Fig. S7 where compartment mobilities were different.